Appl. Magn. Reson. 20, 1–XXX (2001)

February 23, 2001

0105

v.2

Probing the Surrounding of a Cobalt(II) Porphyrin and its Superoxo Complex by EPR Techniques

M. Baumgarten[1], C. J. Winscom[2], and W. Lubitz[3]

[1] Max-Planck-Institut für Polymerforschung, Mainz, Germany
[2] Kodak R&D Ltd, Harrow, Middlesex, Great Britain
[3] Max-Volmer-Institut für Biophysikalische Chemie und Biochemie, Technische Universität Berlin, Berlin, Germany

Received September 26, 2000

Abstract. Octaethylporphyrinato-cobalt(II), Co(II)OEP, was studied by electron paramagnetic resonance (EPR) and electron-nuclear double resonance (ENDOR) in frozen solutions of methanol, tetrahydrofuran and pyridine diluted into chloroform. Oxygenation led to the respective paramagnetic superoxo complexes Co(III)OEPpy$\cdot\cdot O_2^{-\cdot}$. The EPR spectra demonstrate strong differences in the axial ligation states ((base-on)/(base-off)) and ease of the oxygenation process. Additional ENDOR studies with partial orientation selection along the principal g tensor axes are performed for resolution of the ^{1}H, $^{14/15}N$ and ^{59}Co hyperfine (hf) coupling constants. This allows a comparison of the electron spin density distribution of the superoxo complex and its precursor. The data are interpreted in the framework of a more rigorous and detailed theoretical configuration interaction model than previously presented in the literature. The theoretical treatment shows that the structure of the superoxo complex is best described in a three-orbital model with contributions from the cobalt 3d, 4s, and oxygen π orbitals. The analysis reproduces the experimental g and Co hf data yielding the relative energies of the MO's and the MO coefficients for the description of the spin density distribution in the Co(II) complex and its superoxo complex. To demonstrate the generality of the approach and possible applications, a comparison is made with the vitamin B_{12r} system. Furthermore, it provides detailed insight into the electronic and geometric changes resulting from axial ligation and oxygenation of the Co(II)OEP complex; this information can be used for predictions of the catalytic activity.

1 Introduction

Studies of square-planar cobalt(II) complexes have been extensively reported in the literature [1–11] both for their interesting prospects in metal catalysis and as model systems for biologically active species, e.g., vitamin B_{12} [12–16]. Probably the most outstanding property of many cobalt(II) complexes is their ability to form adducts with molecular oxygen [17, 18], which has many implications in chemistry and biology, including catalytic oxidation processes [19–25] and the uptake, transport, storage, and activation of oxygen by heme proteins [26–28].

Systematic approaches to dioxygen activation by metals require insight into the electronic nature of the complexes. Both the cobalt(II) complexes and their dioxygen adducts are particularly well-suited for an investigation of the electronic structure, since they possess at least one unpaired electron, making them ideal for electron paramagnetic resonance (EPR) measurements. Several theoretical models have been published to explain the observed magnetic resonance parameters [29–31].

In most cases, continuous wave (cw) EPR spectroscopy only yields information about the anisotropic g and ^{59}Co hyperfine coupling (hfc) tensors. Superhyperfine (shf) structure from the ligand nuclei can rarely be resolved, since they are usually obscured by the large linewidths met in the powder-type EPR spectra of paramagnetic metal complexes. An exception are ^{17}O hfc's in appropriately labeled dioxygen complexes [26, 32, 33]. In most of the other cases, cw and pulsed electron-nuclear double resonance (ENDOR) spectroscopy are the methods of choice to additionally resolve the interaction of the paramagnetic metal ion with its surrounding magnetic nuclei having nuclear spins $I \geq 1/2$. From the value of these hf interactions one may obtain the electron spin distribution, the distance between the metal and the nuclei and the electric field gradient at the nuclei (for $I \geq 1$), i.e., the intimate electronic details of the metal and its environment.

The successful observation of ENDOR requires saturation of the EPR and nuclear magnetic resonance (NMR) transitions. In most transition metal complexes, also for cobalt(II), spin relaxation rates are very large and EPR saturation becomes a problem at elevated temperatures [34, 35]. Consequently, all our spectra were taken at very low temperatures (<10 K) where the relaxation rates are sufficiently slow to allow a saturation of electron and nuclear spin transitions.

Experiments performed on diamagnetically diluted single crystals yield most information. Many complexes, however, cannot be studied in single crystals because suitable host compounds are hard to find or crystals cannot be grown. Polycrystalline powders or frozen solutions can be prepared much more easily. Single-crystal type ENDOR spectra [36, 37] can be obtained by setting the external magnetic field B_0 at turning points in the EPR spectrum, which correspond to specific canonical orientations of the g or hf tensors with respect to B_0. In the Co(II) complexes studied here, the g anisotropy dominates the spectra and one obtains hf tensor components for the various hf-coupled nuclei along the principal axes of the g tensor. From this information one can, in principle, obtain the location of the nuclei around the spin-carrying metal center (distance $>$ 0.2 nm) [34, 38] by use of the point-dipole approximation as demonstrated earlier for axially ligated Cu(II) and Co(II) complexes [39–43]. More recently cw and pulsed multifrequency EPR and ENDOR studies of Co(II) tetraphenylporphyrin complexes (CoTPP) with imidazol and pyridine as axial ligands as well as their superoxo complexes have been published [8–11]. In this paper we use multinuclear (cw) ENDOR performed on Co(II) octaethylporphyrin (CoOEP) with various ligands as a model (Fig. 1). Particular emphasis is placed on the investigation

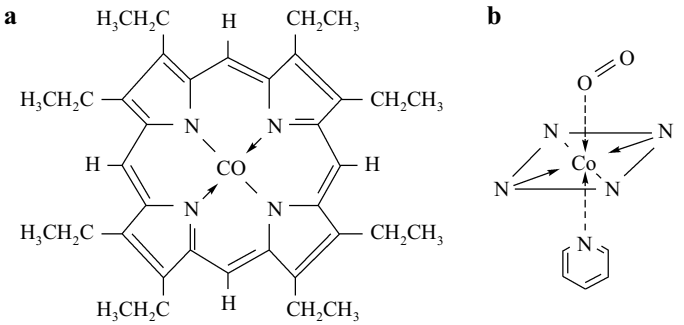

Fig. 1. a Molecular structure of the CoOEP. **b** Sketch of the dioxygen adduct of a square planar cobalt porphyrin with pyridine as axial ligand.

of the different solvent-dependent ligation forms, and on the superoxo complex for which even the ^{59}Co ENDOR resonances could be detected. In addition to the application of established principles [31, 40, 44], the final strength of the procedure used to analyze the electronic structure, especially of the superoxo complex, rests on a more detailed configuration interaction (CI) assessment than previously presented in the literature [29–31].

2 Experimental

2.1 Materials

Octaethylporphyrinato-cobalt(II) (CoOEP) was prepared by reaction of the porphyrin-free base H_2OEP and cobalt(II) acetate (Merck, Darmstadt) [45, 46]. The visible absorption spectrum of the CoOEP was identical to that reported in [47]; EPR/ENDOR samples were prepared in quartz tubes (Wilmad glass o.d. 4 mm) under argon and sealed. Typically, a 10^{-3} M solution of CoOEP was prepared in the required solvent system: tetrahydrofuran (THF) plus toluene (1:1), $CHCl_3$ plus methanol (10:1), or $CHCl_3$ plus pyridine (10:1). All solvents were freshly distilled prior to use and purged with argon for at least 15 min. Isotopically labeled solvents were used as purchased: ^{15}N-pyridine (99.3 atom% ^{15}N, MSD-Isotopes, München), pyridine-d_5 (99 atom% ^{2}H, Janssen, Brüggen), and $CDCl_3$ (99.8 atom% D, Janssen, Brüggen). The oxygenation of the samples was performed for approximately 1 min. The yield of the oxygenated state was monitored by EPR spectroscopy.

2.2 Instrumentation

X-band EPR spectra were recorded on a Bruker ER 200D spectrometer equipped with a Bruker TE_{102} cavity and a variable temperature control unit, 120–400 K

(Bruker 4111 VT). A 100 kHz field modulation with typically 4 G maximum peak-to-peak modulation depth was employed. The microwave frequency was monitored by a frequency counter (Hewlett-Packard, hp 5340). The magnetic field was measured by an NMR gaussmeter (Bruker BNM 12). The calibration of the magnetic field was checked with a phenalenyl standard sample ($g = 2.00262$) [48]. All EPR spectra presented here were measured at $T = 140 \pm 5$ K.

For the low-temperature ENDOR measurements, a Bruker ENB 200 ENDOR cavity (with 12.5 kHz field modulation for the EPR detection), equipped with an Oxford ESR 9 cryostat ($T_{min} = 4$ K) was used. The radio-frequency (rf) channel comprised an rf synthesizer (Hewlett-Packard hp 8660 C), a digital attenuator to provide constant rf power at the sample over the frequency range scanned [49], and an rf amplifier (ENI A300). The latter was loaded by an 18-turn rf coil in series with a power meter and a 50 Ω load. At the maximum rf output (300 W), an rf field of 1.25 mT in the rotating frame could be realized at the sample at 14 MHz (proton Larmor frequency) [50]. 10 kHz frequency modulation (fm) of the rf source allowed ENDOR signals to be recorded as first derivatives of the partially saturated absorption signal. Acquisition of spectral data was performed by a Hewlett-Packard hp 1000 computer, which simultaneously controlled digital attenuation of the rf power. A more detailed description of the instrument can be found elsewhere [51].

All ENDOR spectra were taken at the lowest possible temperature which was slightly dependent on the rf power applied (see figure captions). Another problem was temperature gradients along the samples (30 mm) and sample tubes (170 mm) used to obtain optimum filling factors of the cavity. This was solved by modifying the upper part of the Oxford cryostat, allowing the helium gas to flow along the full length of the sample as it was exhausted.

Optimization of an ENDOR signal proceeded by first varying the microwave power for EPR saturation and subsequently optimizing the rf power and fm modulation depth. The respective optimum values are given in the figure captions.

2.3 Data Analysis

EPR spectra were simulated with a computer program on the basis of a spin Hamiltonian, containing the electronic Zeeman and metal hf interaction [52, 53]:

$$\mathcal{H} = \beta_e \mathbf{B}_0 \mathbf{g} \mathbf{S} + \mathbf{S} \mathbf{A} \mathbf{I} . \quad (1)$$

In this equation **S** and **I** are the electron and nuclear spin operators, β_e is the Bohr magneton, $\mathbf{B}_0$ is the magnetic field, and **g** and **A** are the electronic g and electron-nuclear hf tensors, respectively. In the program, provision was made for noncollinear principal axes of the g tensor and the Co hf tensor [51] and an orientationally-dependent linewidth variation as described earlier [52].

ENDOR frequencies are best interpreted by a nucleus-specific spin Hamiltonian containing the hf, the quadrupole, and the nuclear Zeeman interactions [8,

9, 34, 39–43]. First-order expressions for the ENDOR transition frequencies will approximately hold along g tensor principal directions, if the principal axes of the hf and quadrupole tensors are collinear and, at other orientations, if the hf or Zeeman interaction dominates the nuclear spin Hamiltonian.

For a situation where the magnetic field is aligned along one of the principal axes of the g tensor (for example, g_z), which also happens to coincide with principal axes of the hf (A_z) and quadrupole (Q_z) tensors, the ENDOR transition frequencies are given by:

$$I = \frac{1}{2}: \qquad \nu_{\mathrm{ENDOR}} = \left| \nu_{\mathrm{n}} \pm \frac{A_z}{2} \right|, \tag{2}$$

$$I = 1: \qquad \nu_{\mathrm{ENDOR}} = \left| \nu_{\mathrm{n}} \pm \frac{A_z}{2} \pm \frac{3Q_z}{2} \right|, \tag{3}$$

where ν_{n} is the appropriate nuclear Larmor frequency. The A_z term contains isotropic and anisotropic contributions. The frequency center of the ENDOR spectrum depends on the relative magnitudes of the Larmor, hf and quadrupole terms. Details of higher-order expressions are given in the literature [34, 35].

For protons in transition metal complexes the anisotropic hf interaction is of considerable importance. Provided the electron spin density is distantly localized (>0.2 nm) with respect to the proton (for example, at the metal ion), the anisotropic components are given by

$$A_{\mathrm{aniso}}(z) = g_{\mathrm{n}}\beta_{\mathrm{n}}\beta_{\mathrm{e}}\left(g_{\mathrm{e}}\rho + \frac{\Delta g_z}{r^3} \right)(3\cos^2\vartheta - 1)\,, \tag{4}$$

where g_{n} and g_{e} are the nuclear and free electronic g values, β_{n} and β_{e} are the nuclear and Bohr magnetons, ρ is the distantly localized spin density, and Δg_z is the deviation of the g_z value from the free electron value. The important spatial parameters are r, the vector locating the proton with respect to the localized electron-spin density and ϑ, the angle between r and the z-axis (B_0-axis).

3 Results

3.1 EPR Results

The EPR spectra of Co(II)OEP are significantly different from one another depending on the matrix/solvent used (Table 1). These differences arise mainly as a result of additional axial ligation to the Co(II) ion. Inspection of the values in Table 1 shows that two extreme cases are represented by the Co(II)OEP complex in Ni(II)OEP [54, 55] and Co(II)OEP in frozen pyridine plus $CHCl_3$ solution. In the former, axial coordination, if any, is weak enough to be neglected,

Table 1. Principal values of the g and ^{59}Co hf tensors of Co(II)OEP in various matrices.[a]

Matrices	$g_\perp$	$g_\parallel$	$A_\perp$	$A_\parallel$	References
Ni(II)OEP	3.391	1.599	1361	585	54
Ni(II)OEP	3.390	1.550	1390	61	55
THF[b]	3.352	1.77[d]	1188	605[d]	this work
THF[c]	2.520	2.012	285	317	this work
$CH_3OH/CHCl_3$	2.479	2.024	219	300	this work
Pyridine[e]/$CHCl_3$	2.326	2.025	≤25	231	this work
Pyridine/$CHCl_3$	2.322	2.026	—	234	8

[a] All data from computer simulations of the respective EPR spectra (X-band) in solid matrices at T = 140 K, all spectra interpreted on the basis of axial symmetry of the g and hf tensors, $A_\parallel$ and $A_\perp$ of ^{59}Co given in MHz, errors $g(\pm 0.002)$, $A(\pm 3$ MHz).
[b] "Base-off" state (see text and Fig. 3).
[c] "Base-on" state (see text and Fig. 3).
[d] These values have a larger error because of the superposition of both states, $g(\pm 0.01)$, $A(\pm 10$ MHz).
[e] The nitrogen hfc from the axially coordinated pyridine is $A_\parallel(^{14}N) = 44 \pm 4$ MHz, $A_\parallel(^{15}N) = 60 \pm 4$ MHz, in [8] $A_\parallel(^{14}N) = 1.72$ mT is quoted.

and the situation approaches a pure fourfold coordination for which a particularly large g anisotropy and concomitantly large ^{59}Co hf components are observed. At the other extreme, pyridine as ligand leads to a much smaller g anisotropy and ^{59}Co hf tensor values. Consequently, the EPR spectrum now comprises an unresolved broad feature in the $g_\perp$ region at low field and a still well-resolved eight-line hf pattern in the $g_\parallel$ region (see Fig. 2). The g and ^{59}Co hf tensor components can easily be obtained from a simulation of the spectra (not shown). Coordination of only one pyridine molecule to the Co(II) ion is evident from the three-line ^{14}N ($I_{^{14}N} = 1$) shf pattern centered at each of the $A_\parallel$ (^{59}Co) components. Consequently, the use of ^{15}N pyridine ($I_{^{15}N} = 1/2$) leads to an shf splitting, resulting in two components with equal intensity. Satisfying simulations of both EPR spectra (including the nitrogen) can be achieved (not shown) [51, 56]. Similar results on Co(II) porphyrin complexes have also been reported recently by other authors [8]. A comparison of the EPR data for the methanol plus $CHCl_3$ and the pyridine plus $CHCl_3$ samples leads to the conclusion that in the former also one methanol molecule is axially coordinated (Table 1).

An interesting EPR spectrum is observed in frozen THF solutions. Two pronounced species are detected (Fig. 3a) each of which shows well-resolved eight-line cobalt hf patterns for both principal $g_\parallel$ and $g_\perp$ regions. The simulated spectra of the two component species are shown in Fig. 3b and c, respectively. A comparison with Co(II)OEP data in other matrices (see Table 1) shows that the two species in THF may be classified as follows.

The species whose characteristics are similar to those of the complex diluted in a diamagnetic Ni(II)OEP host [54, 55] is regarded as the "base-off" state; whereas, the species whose spectrum is similar to that in methanol is regarded

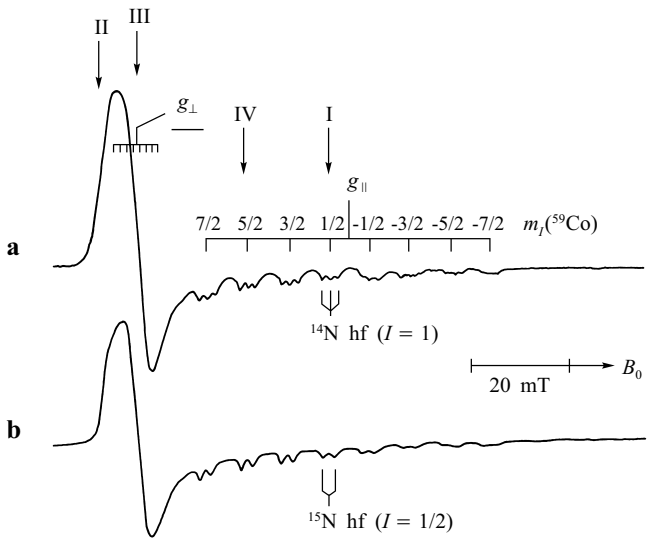

Fig. 2. EPR spectra (X-band) of Co(II)OEP with **a** ^{14}N pyridine and **b** ^{15}N pyridine as axial ligands, respectively, in chloroform at $T = 140$ K (frozen solution), concentration 10^{-3} M, field modulation (100 kHz) amplitude 0.4 mT (peak-to-peak), microwave (mw) power 20 mW, recording time 200 s. The cobalt hf structure, $I(^{59}Co) = 7/2$, is resolved for $g_\parallel$. The shf splitting in this region arises from the coupling of the unpaired electron at the Co(II) with one nitrogen atom, **a** $I(^{14}N) = 1$ and **b** $I(^{15}N) = 1/2$. The g and Co hf data are given in Table 1. The Roman numbers I, II, III and IV indicate selected field positions for which ENDOR spectra were obtained (see Figs. 5 and 6).

as the "base-on" state (Table 1). The "base-off" state shows varying distances of the Co hf lines due to large second-order effects as deduced from the simulation shown below. The addition of toluene – or use of a toluene/THF (1:1) mixture – leads to the disappearance of the "base-off" state, leaving predominantly the "base-on" state. The unpolar toluene cage obviously forces the more polar THF molecules to bind to the charged metal ion.

The axially ligated Co(II) complexes can easily be oxygenated with the procedure outlined in the Sect. 2. With THF, the oxygen is only loosely bound. The fivefold coordinated species takes up oxygen preferentially [31], which is demonstrated by its reduced intensity in the resulting EPR spectrum leaving three overlapping species: the "base-on", the "base-off", and the superoxo form. A more detailed analysis is difficult as a result of the two competing equilibria between the four- and fivefold coordinated species on the one hand, and the fivefold coordinated species and the oxygenated one on the other. The complex can be deoxygenated quite easily by flushing the sample with argon for several minutes. With methanol, a complete uptake of oxygen occurs, but the hf components in the EPR spectrum of the superoxo complex are poorly resolved. In the presence of pyridine, however, a well-resolved EPR spectrum of the fully oxygenated complex is observed (Fig. 4). This spectrum is characterized by an order of magnitude reduction of the g anisotropy and the ^{59}Co hf splitting com-

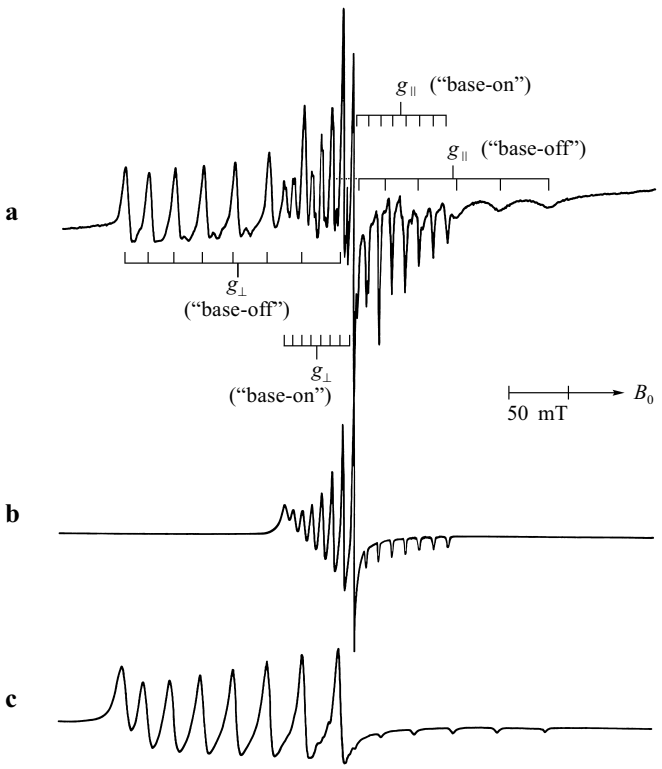

Fig. 3. a EPR spectrum (X-band) of Co(II)OEP in THF at $T = 140$ K, for experimental conditions see Fig. 2 (recording time 1000 s). The simulations for **b** the "base-on" and **c** the "base-off" states are shown. The line positions are in very good agreement but the linewidths are less well reproduced by the simulation. Both states are superimposed in the experimental spectrum (**a**). Note that the large hf interactions lead to strong second-order effects resulting in unequal hf line spacings at each g direction. The g and Co hf data are given in Table 1.

pared with those of its deoxy precursor (compare Figs. 2 and 4). Such effects are typical for Co(III)-superoxo complexes in which the unpaired electron (upe) mainly resides in the dioxygen ligand [31, 57].

In Fig. 4, the EPR spectrum of $Co(III)OEP \cdot py \cdot O_2^{-\bullet}$ in $CHCl_3$ is shown together with the simulated spectrum and the axes system chosen. The EPR spectrum exhibits a rhombic g tensor, indicating a reduction in symmetry. No nitrogen hf couplings can be resolved even when using ^{15}N pyridine. For the simulation of the powder spectrum, it was anticipated that the principal axes of the g tensor are not collinear with the principal axes of the ^{59}Co hf tensor [31]. Analysis, therefore, proceeded by considering one common collinear axis and a rotation of the g axes system by angle α with respect to the ^{59}Co hf axes system about this axis (Fig. 4c). The choice of α is not unambiguous. A simulation with $\alpha = 0$ gave values of 55, 31 and 26 MHz for A_x $(=A_{g_{y'}})$, A_y $(=A_{g_{z'}})$ and A_z $(=A_{g_{x'}})$, respectively. The range of values measured by ^{59}Co ENDOR (see

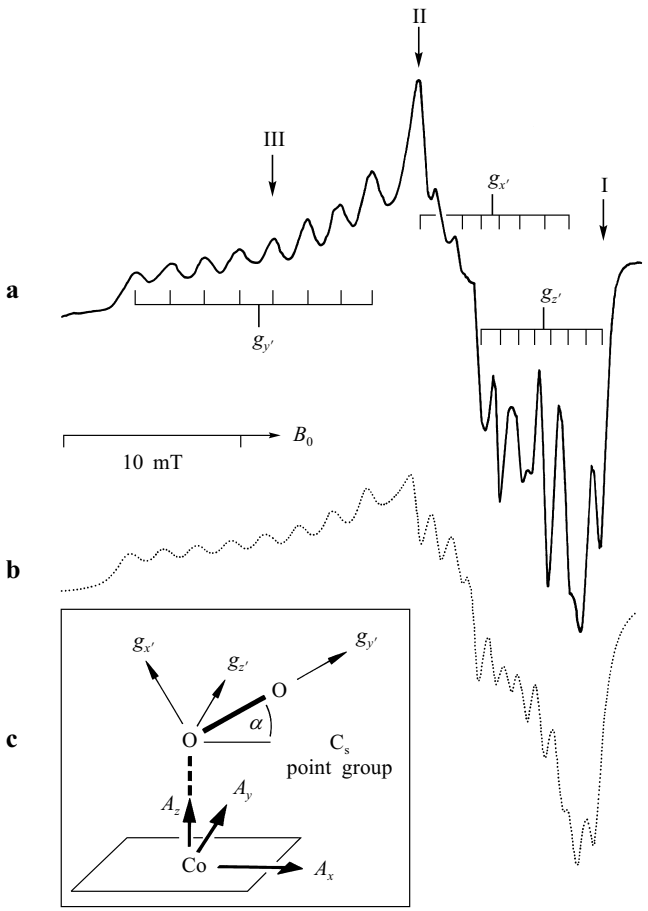

Fig. 4. a EPR spectrum (X-band) of Co(III)OEP · py · $O_2^{-\bullet}$ in chloroform at $T = 140$ K, concentration 10^{-3} M, field modulation amplitude 0.125 mT (peak-to-peak), mw power 20 mW, recording time 200 s. The Roman numbers I, II and III indicate the field positions for which ENDOR spectra are shown (see Figs. 7–10). **b** Computer simulation [51] with the g and Co hf tensor components given in Table 4 and an angle $\alpha = 22°$ (see **c**); **c** shows the axes system used for the description of this complex and specifies the angle α. In contrast to the nonoxygenated species, the axes for the g and Co hf tensors are not collinear, they are given by i' and i ($i = x, y, z$), respectively.

below) showed, however, that α cannot be zero. The best value is $\alpha = 23°$ for which 59, 26, and 22 MHz are obtained [31] for the principal value of the ^{59}Co hf tensor A_x, A_y and A_z, respectively (cf. Sect. 3.3). The simulation shown in Fig. 4b was obtained for $\alpha = 23°$. The g and ^{59}Co hf-tensor values of the Co(III)OEP · py · $O_2^{-\bullet}$ complex and its deoxy precursor have been obtained from the spectra (see Table 4). These values are in good agreement with those found by van Doorslaer and Schweiger [10] and also Bowen et al. [11] for oxygenated CoTPP complex, who also pointed out temperature-dependent changes of the g anisotropy due to oxygen rotation at liquid nitrogen temperature (100–200 K).

3.2 ENDOR Results of Co(II)OEP

A particularly important consideration for the ENDOR experiments is the strategy by which specific molecular orientations are selected via the EPR powder pattern. For a given resonance field, B_{res}, within this powder spectrum it is already clear from the first-order expression

$$B_{res} = \frac{h\nu - m_I A(\delta, \varphi)}{\beta_e g(\delta, \varphi)}, \tag{5}$$

that solutions of δ and φ (specific orientations) are m_I-dependent, theoretically one obtains $(2I + 1)$ solutions. In the Co(II) and Co(III) $\cdot O_2^{-\bullet}$ species studied here ($I_{^{59}Co} = 7/2$), orientations become very specific at the extreme limits of the spectra (see Fig. 2); i.e., for the high-field extreme ($g_{\|}$, $m_I = -7/2$) one would, in principle, obtain single-crystal type ENDOR spectra. On other m_I components of $g_{\|}$ one retains predominantly the extreme orientations but could have contaminations from other orientations. For the low-field extreme ($g_{\perp}$) a two-dimensional ENDOR powder pattern is observed since g_x and g_y are not clearly separated in X-band.

3.2.1 ^{1}H ENDOR

The proton ENDOR spectra of the Co(II)OEP in deuterated pyridine-d_5 plus chloroform-d_1 (1:10) enable a clean assignment of proton couplings stemming from the porphyrin ligand and separation from solvent and axial ligand effects, since the deuteration also leads to a sharpening of the central portion of the spectrum, which is indicative for the loss of proton resonances from the surrounding matrix. With $B_0 \| z$ ($m_I(^{59}Co) = 1/2$; EPR position I), the intense signals around the proton Larmor frequency yield splittings of 0.98 and 0.36 MHz (Fig. 5c); they must be due to the sets of 4 methine (meso) and 16 ethyl (CH_2) protons. The CH_3 proton hfc's of the ethyl groups are probably too small for detection. For EPR field settings on the strong perpendicular signal at $g_{\perp}$ (position II, Fig. 2) only one very strong signal together with a shoulder is obtained, yielding splittings of 0.87 and 0.38 MHz (Fig. 5d). The small proton hf couplings are in agreement with the relatively large distance to the spin carrying cobalt ion (~0.45 nm for the methine and 0.56 nm for the methylene protons) and the negligible spin density in the $d_{x^2-y^2}$ orbital. These strong proton signals in the center are also observed upon use of protonated pyridine (Fig. 5a, b) where the additional less intense ^{1}H ENDOR signals are now assigned to the pyridine ligands (Table 2). Since large proton couplings may overlap with ^{14}N resonances from the pyridine the proton ENDOR spectra were also measured with py-^{15}N. In these experiments, a maximum proton contribution (8.8 MHz) is found in powder type perpendicular orientations (not shown, most probably including the Co-H director). This is in agreement with data by Däges and Hüttermann [8] and van Doorslaer

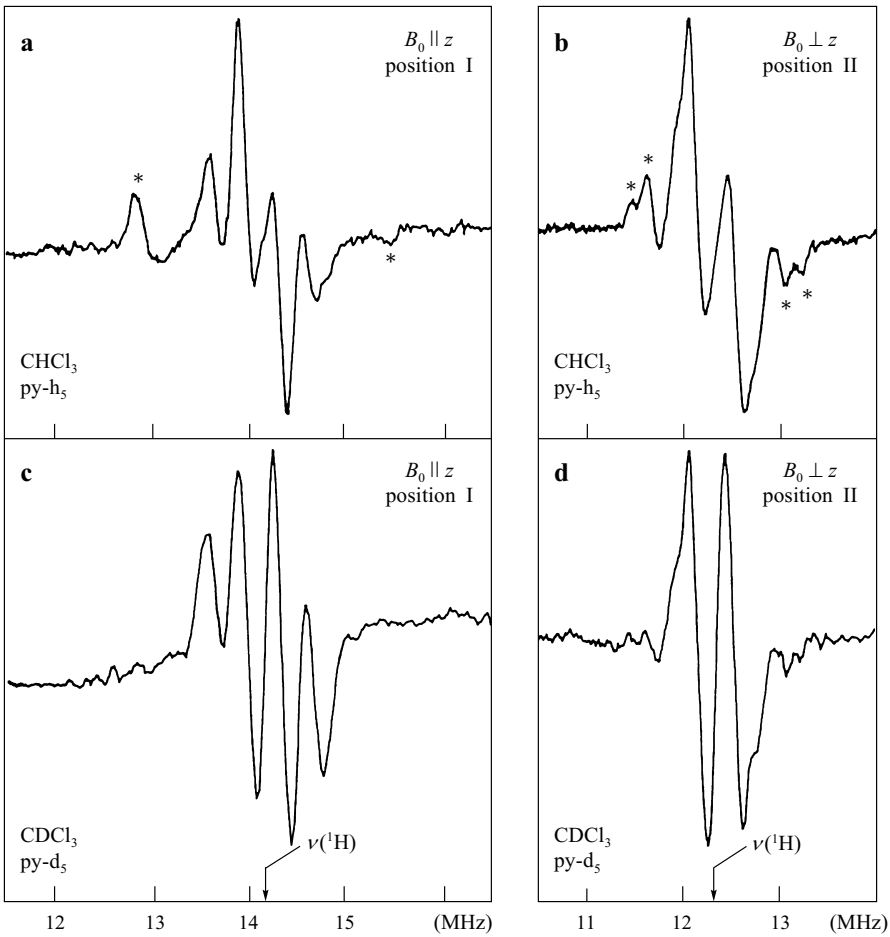

Fig. 5. ^{1}H ENDOR spectra of Co(II)OEP **a**, **b** in a 1:10 mixture of pyridine plus chloroform and **c**, **d** in pyridine-d_5 plus chloroform-d_1 at $T = 10$ K; mw power 4 mW, rf power 60 W, 10 kHz fm with ± 50 kHz deviation, 20 scans (5 s/MHz). For EPR positions I and II refer to Fig. 2. The ^{1}H ENDOR lines (**a**, **b**) belonging to pyridine protons are marked by asterisks; they are absent in traces **c** and **d**. Note that at the perpendicular orientation a larger coupling belonging to the pyridine protons was detected (not shown), see text.

et al. [9] who reported that the pyridine-ortho protons (positions 2 and 6) in CoTPP-py give rise to very large couplings of 8.6 and 7.0 MHz, respectively.

Also the proton ENDOR spectra for the parallel and perpendicular orientations of CoOEP in THF plus toluene (base-on) were taken. Besides the proton signals of the OEP again larger proton couplings for the THF protons are found, very similar to those measured earlier in a Co(dmgh)$_2$ complex [39]. For $B \perp z$, the couplings of 2.85, 2.00, and 1.50 MHz and for $B \| z$ couplings of 2.5 and 1.4 MHz are assigned to THF. These data were analyzed by us in an earlier publication on Co(dmgH)$_2$ [39]. A very similar orientation of the THF molecule

Table 2. Hyperfine data from Co(II)OEP in pyridine plus $CHCl_3$ measured by ENDOR (in MHz).[a]

Nucleus	Assignment	$\|A_\perp\|$	$\|A_\parallel\|$
^1H	H (pyridine)	8.80, 1.76, 1.38	2.57
	H (OEP, ethyl)	0.87	0.36
	H (OEP, meso)	0.38	0.98
	H (THF)	2.85, 2.00, 1.50	2.5, 1.4
^{15}N	^{15}N (pyridine)	54.0	60.0
^{14}N	^{14}N (pyridine)	38.5	42.8

[a] A_i ($i = \parallel, \perp$) are the dipolar hf tensor elements, measured in the g tensor axes system (see text); error (^1H hfc's) ± 0.03–0.05 MHz, error (N hfc's) ± 1.0 MHz. For a simulation of the nitrogen ENDOR spectra see [56].

relative to the square-planar Co(II) complex to that determined earlier for THF ligation to $Co(dmgH)_2$, can be assumed [39] for the case of CoOEP.

3.2.2 Nitrogen ENDOR

For the investigation of the nitrogen hfc from the axially coordinated pyridine, ^{15}N is the nucleus of choice, since it has no quadrupole moment ($I(^{15}N) = 1/2$) and, therefore, gives simpler ENDOR patterns (see Eqs. (2) and (3)). In Fig. 6, the ^{15}N ENDOR spectra are shown for the $B_0 \perp z$ (a) and $B_0 \parallel z$ (b) directions (positions II and I in the EPR, see Fig. 2). According to the ENDOR resonance condition only two lines are obtained for both field settings. For the $B_0 \parallel z$ orientation, the two lines are separated by $2\nu(^{15}N) = 2.88$ MHz. The hfc cannot be obtained very precisely because of the peculiar lineshapes; an approximate value is $A_\parallel(^{15}N) = 60.0 \pm 1.0$ MHz, which is in very good agreement with the value of 60.9 ± 1.0 MHz obtained from the simulation of the ^{15}N ENDOR line shapes [56] and with the approximate value deduced from EPR (60 ± 4 MHz), see Fig. 2b.

For the $B_0 \perp z$ region, a ^{15}N hf splitting is not resolved in the EPR and can only be obtained from ENDOR. Here, the two lines are separated by $2\nu(^{15}N) = 2.45$ MHz, and the obtained value is $A_\perp(^{15}N) = 54.0 \pm 1.0$ MHz. Desaturation of various parts of the $B_0 \perp z$ region in the EPR (e.g., positions II and III, Fig. 2) consistently yields the same well-resolved ^{15}N ENDOR spectrum very similar to that shown in Fig. 6a. From these experiments, it is concluded that the ^{15}N hf tensor is very close to being axially symmetric, since otherwise one would expect line shift and/or line broadening in the spectra. From the ^{15}N hfc's the ^{14}N values can be calculated by multiplication with $\gamma(^{14}N)/\gamma(^{15}N) = -0.713$ (γ is gyromagnetic ratio).

^{14}N pyridine ($I(^{14}N) = 1$) as axial ligand leads to contribution of the quadrupole interaction in addition to that from the anisotropic hf splitting in the nitro-

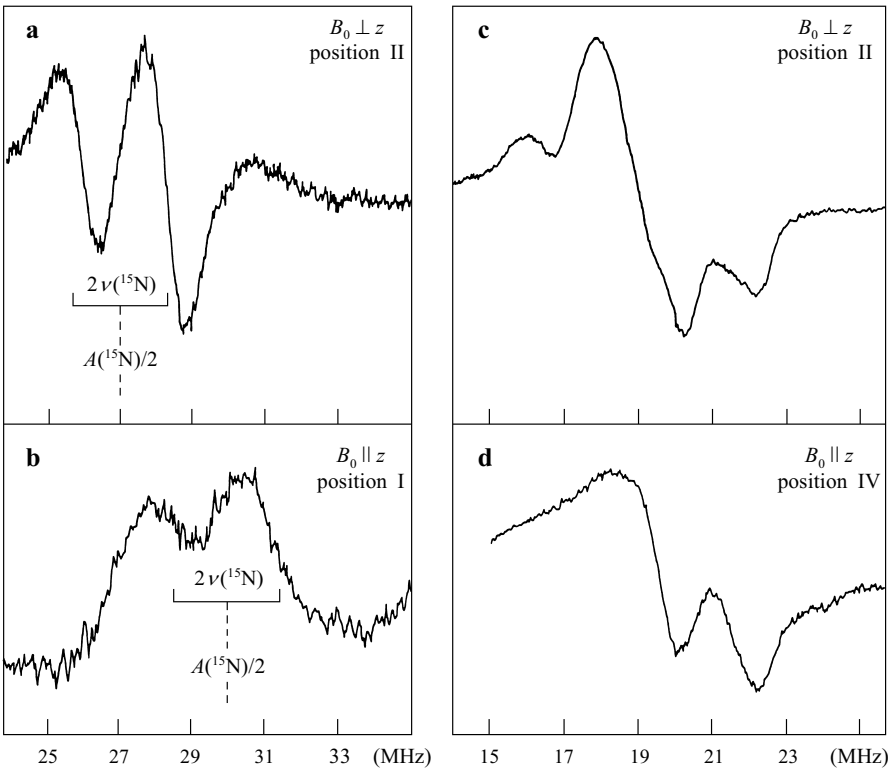

Fig. 6. a, **b** ^{15}N ENDOR spectra of Co(II)OEP in ^{15}N-pyridine plus chloroform (1:10), $T = 7\pm2$ K, mw power 20 mW, rf power 100 W, 10 kHz fm with ±120 kHz deviation, 10 scans each (2.5 s/MHz); **c**, **d** ^{14}N ENDOR spectra of Co(II)OEP with ^{14}N pyridine plus chloroform (1:10), conditions as for ^{15}N, except for rf power 80 W. Note the shift in resonance position and the additional splitting (**c**) due to the quadrupole interaction. For EPR positions I, II and IV see Fig. 2.

gen ENDOR spectra (see Eq. (3)) (Fig. 6c and d). As shown by van Doorslaer et al. [9] the measurement and analysis is very difficult. The resolution from X-band ENDOR is probably not sufficient since overlap with proton signals is obtained which prevents a reliable analysis of the quadrupole couplings. An earlier simulation including the quadrupole interaction [56] must therefore be reconsidered, since the $Q_{\parallel}$ value should be the largest, which is not the case in [56]. With the gyromagnetic ratios, the ^{14}N couplings can be calculated from the ^{15}N hfc's yielding $A_{\perp}(^{14}N) = 38.5$ MHz and $A_{\parallel}(^{14}N) = 42.8$ MHz. The latter value agrees with that obtained from EPR (44 ± 4 MHz) in Fig. 2a.

Since the four pyrrole nitrogens are lying in the *xy*-plane of the complex that has the upe in the d_{z^2} orbital, only small ^{14}N hfc's are expected for these nuclei. Such resonances are observed in the low-frequency region (1–7 MHz) but an analysis of the observed resonances was not possible by our technique. Here, the additional advantages of pulsed multifrequency techniques proved to be useful [9–11], but some lines are still below the detection limit [9]. Resonances from

the ^{59}Co nucleus in Co(II)OEP could not be observed in any of our ENDOR spectra.

3.3 ENDOR of Co(III)OEP · py · $O_2^{-\bullet}$

The EPR field positions in the cobalt superoxo state are not directly comparable with the cobalt(II) complex, since the *g* tensor axes system is now referred to the spin-carrying dioxygen ligand and no longer to the cobalt ion. Orientation selection, therefore, yields hf tensor components along the new primed *g* tensor axes system (Fig. 4c).

As mentioned above, the EPR spectrum of the oxygenated CoOEP in pyridine plus $CHCl_3$ is characterized by drastically reduced *g* and ^{59}Co-tensor values (Fig. 4). Thereby the relaxation characteristics are also changed, resulting in reduced EPR linewidths (~20 MHz) and less stringent saturation requirements for cw ENDOR experiments. This makes this system a much better candidate for ENDOR spectroscopy than the Co(II)OEP complex. Indeed, various nuclei are indicated in the 1 to 20 MHz ENDOR range under the same experimental conditions. One

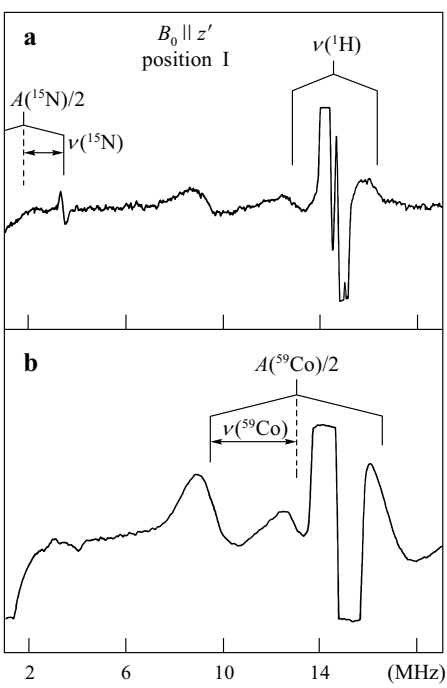

Fig. 7. Multinuclear (^{1}H, ^{15}N, ^{59}Co) ENDOR spectra of Co(III)OEP · py(^{15}N) · $O_2^{-\bullet}$ for $B_0 \| z'$ (EPR position I, Fig. 4) in ^{15}N pyridine plus chloroform; $T = 10$ K, mw power 20 mW, rf power 80 W, 10 kHz fm deviation **a** ±80 kHz and **b** ±600 kHz. The Larmor frequencies and hfc's for **a** ^{15}N, ^{1}H and **b** ^{59}Co are indicated (see ENDOR resonance conditions Eqs. (2) and (3)), for further proton resonances near $\nu(^1H)$ see Fig. 8.

spectrum is shown in Fig. 7a as an example, which was obtained at position I in the EPR spectrum (Fig. 4), $B_0 \| z'$. The proton resonances occur as very intense lines around the Larmor frequency, $\nu(^1\mathrm{H}) = 14.60$ MHz. Their linewidths are only 100 to 200 kHz, requiring a low field-modulation depth for resolution (± 50 kHz). Their intensity is almost one order of magnitude larger than that of the other lines in the spectrum. However, there are other types of proton resonances exhibiting very broad and much less intense lines at about 13 and about 16 MHz; they belong to a different type of protons. Furthermore, a fairly sharp (200 kHz) but weak line is detected at 3.45 MHz which is assigned to the high-frequency ^{15}N resonance of the axial ligand (^{15}N pyridine). The low frequency counterpart should occur in a distance of twice the ^{15}N Larmor frequency, $\nu(^{15}\mathrm{N}) = 1.48$ MHz; i.e., at 0.49 MHz, which is outside the useful range of the ENDOR spectrometer. Furthermore, resonances from the ^{59}Co nucleus (natural abundance 100%) could be detected. They occur around $A(^{59}\mathrm{Co})/2 = 12.6$ MHz and are spread apart by twice the ^{59}Co Larmor frequency, $\nu(^{59}\mathrm{Co}) = 3.44$ MHz. No quadrupole splitting could be resolved since these lines are quite broad (≥ 1 MHz) obscuring additional splittings. In Fig. 7b, a spectrum is shown in which a higher fm modulation depth (± 600 kHz) was used, appropriate for optimum detection of the ^{59}Co ENDOR lines. In this trace the proton resonances are severely broadened, and the ^{15}N line is even split by the large modulation amplitude. A more detailed analysis of the resonances of the various nuclei is given below.

3.3.1 ^{1}H ENDOR

The ^{1}H ENDOR spectra of the oxygenated samples are shown in Fig. 8a–c for the outermost field position, $B_0 \| z'$. Three pairs of lines are detected. One pair presents itself as shoulders of the inner lines. Inspection of the ENDOR spectra at other g components in the z', x' and y' directions shows only small changes indicating largely isotropic proton hf interactions. Deuterated pyridine (Fig. 8b) leads in all spectra to the disappearance of the line pair having the largest coupling, which is attributed to the α protons of the pyridine. A small decrease of this coupling is observed by going from the $g_{y'}$ to the $g_{z'}$ direction ($A_{g_{y'}} = 1.17$, $A_{g_{x'}} = 1.07$, $A_{g_{z'}} = 1.02$ MHz). The remaining two inner line pairs are assigned to the meso and ethyl(CH_2) protons of the porphyrin.

In the spectral range shown in Fig. 8, the use of deuterated chloroform (Fig. 8c) affects only the intensity of the signals near the free proton frequency (matrix region), indicating interaction with some weakly coupled solvent protons. Inspection of a wider spectral range in protonated solvents, however, reveals more proton line pairs (at least 2) centered around $\nu(^1\mathrm{H})$ with larger hfc's, These are indicated in Fig. 7a for the $B_0 \| z'$ direction. The lines are very broad and weak in intensity and somewhat change position and amplitude for various field positions. Precise determination of these couplings is frustrated by overlapping ^{59}Co signals for the $g_{x'}$ and $g_{y'}$ field director; the hfc's are collected in Table 3. All the lines disappear completely when deuterated solvents ($CDCl_3$/py-d_5) are used.

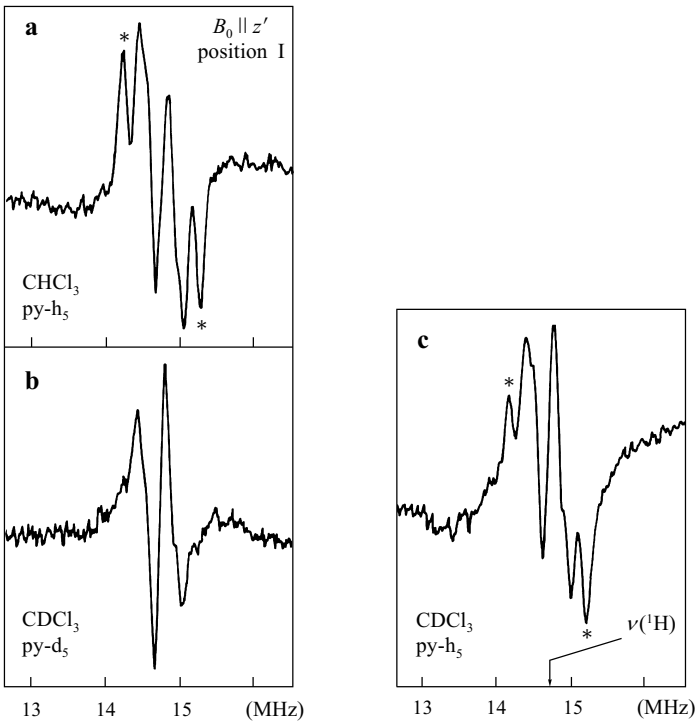

Fig. 8. ^{1}H ENDOR spectra of Co(III)OEP · py · $O_2^{-\bullet}$ for $B_0 \| z'$ (EPR position I, Fig. 4) with **a** pyridine plus chloroform, **b** pyridine-d_5 plus chloroform-d_1, and **c** pyridine plus chloroform-d_1; $T = 10$ K, mw power 2.2 mW, rf power 50 W, 10 kHz fm deviation ±40 kHz, 20 scans (5 s/MHz). The resonances belonging to protons from the pyridine are marked by asterisks (**a**, **c**).

Table 3. Hyperfine data from Co(III)OEP · $O_2^{-\bullet}$ in pyridine/$CHCl_3$ measured by ENDOR (in MHz).[a]

Nucleus	Assignment	$A_{x'}$	$A_{y'}$	$A_{z'}$	Error
^{1}H	ortho-H (pyridine)	1.07	1.17	1.02	±0.03
	H(OEP, ethyl)	0.6	0.52	0.6	±0.05
	H(OEP, meso)	0.4		0.4	±0.05
	$CHCl_3$[b]	5.6	5.0[c]	5.8[c]	±0.1
		4.0	3.2	3.8	±0.1
^{15}N	^{15}N (pyridine)	3.92	3.87	3.93	±0.05
^{59}Co	Cobalt	22	59	26[d]	±3.0

[a] A_i ($i = x', y', z'$) are the hf tensor elements of the various nuclei measured in the g-tensor axis system, see Fig. 4c. For ^{59}Co it is concluded that values close to the principal values A_z, A_x and A_y are captured in the ENDOR spectra (see text).

[b] From solvent molecules surrounding the $O_2^{-\bullet}$ moiety.

[c] These splittings occur as shoulders on the main line.

[d] This value is the most accurately determined one (error ±1 MHz).

Therefore, they are assigned to protons in the surroundings of the spin-carrying dioxygen ligand. This is supported by the fact that ^{1}H hfc's of comparable magnitude are not observed in the parent deoxy complex. The large linewidths are indicative of some disorder in the position of the protons. It is not clear if these resonances belong to several protons or to specific ones forming a hydrogen bond between the solvent ($CHCl_3$) and the oxygen. Such large proton couplings were also obtained in oxy hemoglobin and interpreted as stemming from hydrogen bridges between the protein matrix and the spin-carrying oxygen [58].

3.3.2 Nitrogen ENDOR

In the EPR spectra of the oxygenated sample no nitrogen hf signals are resolved. Thus, their magnitudes must be reduced compared with the cobalt deoxy state and are now smaller than the EPR linewidth (<20 MHz). In Fig. 9a and c, the

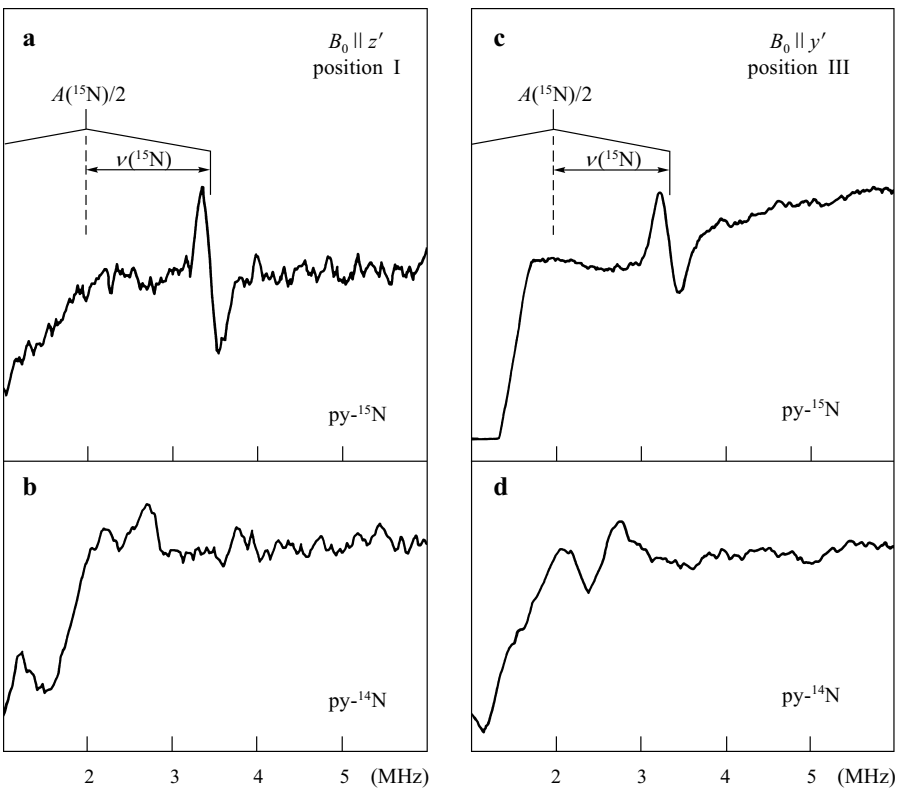

Fig. 9. ^{15}N and ^{14}N ENDOR spectra of Co(III)OEP · py · $O_2^{-\bullet}$ with ^{15}N- and ^{14}N-pyridine, respectively (1:10 in chloroform), $T = 7 \pm 2$ K, mw power 20 mW, rf power 70 W, 10 kHz fm deviation ±100 kHz, 10 scans (5 s/MHz). Traces **a**, **b** and **c**, **d** compare the ^{15}N and ^{14}N spectra obtained at the same EPR field position (I and III, respectively) indicated in Fig. 4.

^{15}N ENDOR spectra of the oxygenated complex with ^{15}N-pyridine as axial ligand are shown. For all field orientations (including $B_0 \| x'$, not shown) a sharp line (linewidth ca. 200 kHz) is detected near 3.4 MHz. No other such lines are detected at higher frequencies. Since this line disappears when ^{14}N pyridine is used as base, it is attributed to the high-frequency resonance of the ^{15}N nucleus. The low-frequency counterpart is expected below 1 MHz and is thus not accessible. By use of the known ^{15}N Larmor frequency, the ^{15}N hfc can be obtained (see Table 3). It shows only a very small orientation dependence; i.e., it is almost completely isotropic.

With ^{14}N pyridine (Fig. 9b and d) several lines are detected at lower frequencies. These lines, however, turn out not to be sufficient for additional resolution of the quadrupole coupling.

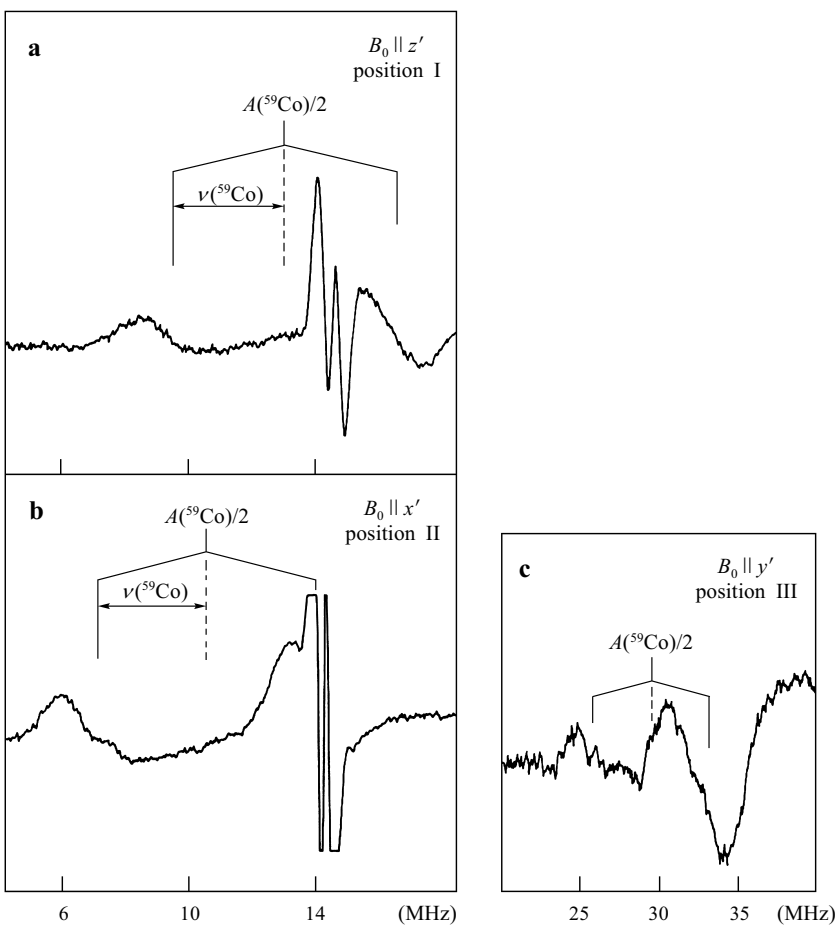

Fig. 10. ^{59}Co ENDOR spectra of Co(III)OEP · py · $O_2^{-\bullet}$ in chloroform for three different field positions **a** I, **b** II and **c** III in the EPR spectrum (see Fig. 4); $T = 7 \pm 2$ K, mw power 20 mW, rf power 80 W, 10 kHz fm deviation **a**, **b** ± 120 kHz and **c** ± 600 kHz.

3.3.3 ^{59}Cobalt ENDOR

Analysis of the EPR spectrum by computer simulation (Fig. 4) already yielded information about the ^{59}Co hf tensor (see above). Additional ENDOR experiments offer the possibility to support the assignments, to measure the hfc's with higher accuracy and, together with the EPR data, allow a determination of the angle α. Furthermore, some information about the quadrupole couplings might be expected. ^{59}Co ENDOR lines could be detected for all three orientations marked in Fig. 4. For directions I, II (Fig. 10a, b) the high-frequency ^{59}Co line interferes with the broad matrix-proton lines from the solvent (see above). All spectra show fairly broad lines, the linewidths are approximately 1.5 MHz in Fig. 10a and b and approximately 3.5 MHz in Fig. 10c. In the latter spectrum ($B_0 \| y'$) the lines are quite weak. In all cases the resonances appear around $A(^{59}\mathrm{Co})/2$ in a distance of $2\nu(^{59}\mathrm{Co})$ indicated in the spectra. The values obtained for the ^{59}Co hf tensor are: $|A_x| = 59 \pm 3$ MHz, $|A_y| = 26 \pm 1$ MHz, and $|A_z| = 22 \pm 3$ MHz. These agree quite well with the EPR analysis with $\alpha = 23°$. We therefore consider these values to be close to the principal tensor values (Table 4). The values are, however, not very accurate due to the large linewidth and due to a variation depending on the exact field position used in the spectra). The observed shoulder in Fig. 10b could be due to quadrupolar effects. A comparison with the values given by van Doorslaer et al. [10] for $\mathrm{CoTPP} \cdot \mathrm{py} \cdot \mathrm{O_2}$ ($A_x = -53.0$ MHz, $A_y = -21.4$ MHz, $A_z = -22.7$ MHz) show a satisfactory agreement keeping the somewhat different molecular system in mind. The angles of the Co-O-O bond are also quite similar (23° in our work versus 26° in [10]). Note that van Doorslaer and Schweiger [10] are using a somewhat different axis system for their superoxo complex.

4 Discussion

The overarching goal of this study has been to obtain a better understanding of the electronic and geometrical structure of the superoxo complex. The ligand-based multinuclear ENDOR results are best discussed when an adequate description of the electronic structures for the Co(II) complex and its $\mathrm{Co(III)} \cdot \mathrm{O_2^{-\bullet}}$ counterpart is to hand. The broad features of their electronic structures, namely the location of the main portions of the spin density and the approximate location of the low-lying excited states, can be deduced from their respective g and ^{59}Co hf tensors.

The Co(II) species is considered first; the general electronic description is already well-understood [44] and is dealt with only briefly. The EPR and ENDOR results are interpreted on this basis, and the fine details won from their analyses lay the foundation for discussing the superoxo counterpart. The subsequent treatment of the $\mathrm{Co(III)} \cdot \mathrm{O_2^{-\bullet}}$ warrants a more thorough approach to the description of the electronic structure, because some general characteristics are still poorly understood. Intuitively, it should be a consistent extension of that for its Co(II) precursor, and this is the approach taken.

4.1 Electronic Structure of Co(II)OEP · py

The molecular orbital (MO) level ordering used to interpret square-planar Co(II) complexes is that shown on the left-hand side of Fig. 11. Only the levels relevant to the EPR interpretation, namely those of mainly metal 3d-character, are shown. The upe resides in an MO of mainly $3d_{z^2}$ character and is the highest occupied orbital of Co(II)OEP · py. Its form is more precisely given by:

$$|\phi_{z^2}\rangle = \alpha_d|3d_{z^2}\rangle + \alpha_s|4s\rangle - \alpha_l|lig\rangle\,, \tag{6}$$

where α_d and α_s are the coefficients corresponding to the $3d_{z^2}$ and 4s atomic orbitals (AO's) and α_l is the coefficient for a delocalized ligand orbital $|lig\rangle$ of A_{1g} symmetry under the C_{4v} point group. Orthonormalization, assuming negligible metal-ligand overlap, requires that $\alpha_l^2 = 1 - \alpha_d^2 - \alpha_s^2$. Within the limit of EPR resolution, Co(II)OEP · py exhibits cylindrical symmetry which is consistent with the above description.

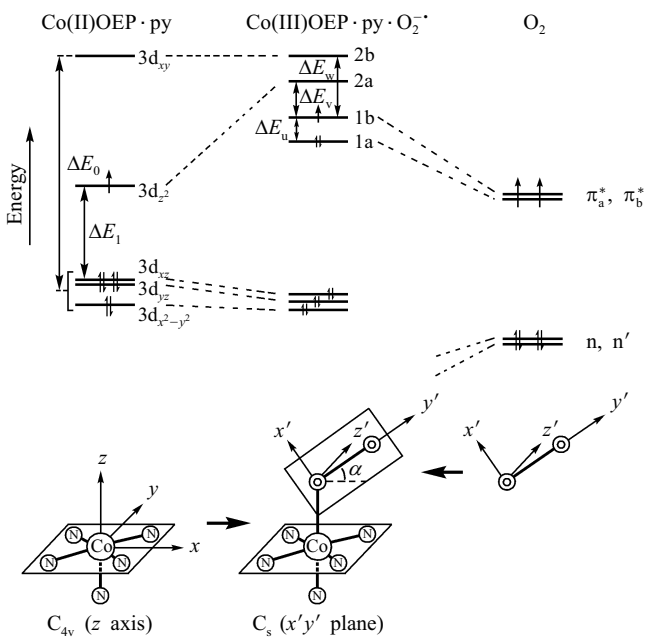

Fig. 11. MO level scheme for Co(III)OEP · py · $O_2^{-\bullet}$. The important MO energy levels and their relationship to those of their precursors in Co(II)OEP · py and O_2 on the left- and right-hand sides of the diagram, respectively, are shown. The energy differences ΔE_0, ΔE_1, ΔE_u, ΔE_v and ΔE_w referred to in the text are indicated. The energy differences ΔE_3 and $\Delta E_3'$ referred to in the text are omitted in this diagram, since they involve more complex excited states not representable by the promotion of a single electron. The relationship between the x', y', z' axes system of the O_2 moiety and the x, y, z axes system for the Co(II)OEP · py precursor is depicted at the bottom of the figure. n, n′ are the nonbonding sp hybrids at the oxygen atom bound to cobalt, and at the terminal oxygen atom, respectively.

Since the anisotropic g shifts deviate from the free electron value (g_e) by less than 0.33, they are not excessive for a square-planar cobalt(II) complex, and the perturbation approach proposed by McGarvey [44] is appropriate. Convenient expressions relating the principal values of the g and ^{59}Co hf tensors to 3d and 4s spin densities, and the energies of the low-lying doublet and quartet excited states for the more general (C_{2v}) case, have been described previously [53]. The C_{4v} case is simpler; in terms of the notation of [44]:

$$\Delta g_\perp + \frac{1}{6}\Delta g_\perp^2 \approx 6\alpha_d^2 c_1 + \frac{2}{3}c_3^2, \tag{7}$$

$$\Delta g_\parallel + \frac{1}{12}\Delta g_\perp^2 \approx 2c_3^2, \tag{8}$$

$$A_\parallel + \frac{1}{7}P\Delta g_\perp \approx K + \frac{4}{7}P\alpha_d^2 - \frac{4}{7}(c_3 - c_3'), \tag{9}$$

$$A_\perp - \frac{15}{14}P\Delta g_\perp \approx K - \frac{2}{7}P\alpha_d^2 + \frac{2}{7}(c_3 - c_3'), \tag{10}$$

where K is the Fermi contact interaction, comprising contributions from the metal 3d and 4s spin densities given by:

$$K = \alpha_d^2 K_d + \alpha_s^2 K_s. \tag{11}$$

For the Co(II), ion $K_d = -85 \cdot 10^{-4}$ cm^{-1} [44] and $K_s = +1220 \cdot 10^{-4}$ cm^{-1} [59], $P = g_e\beta_e g_n\beta_n\langle r_{3d}^{-3}\rangle$ and for the Co(II) ion has the value $220 \cdot 10^{-4}$ cm^{-1} [60]. The remaining coefficients are:

$$c_1 = \frac{\zeta}{\Delta E_1}, \tag{12}$$

$$c_3 = \frac{\zeta}{\Delta E_3}, \tag{13}$$

$$c_3' = \frac{c_3}{1 + 29c_3}, \tag{14}$$

in accordance with McGarvey's definitions in [44]. The spin-orbit coupling constant for Co(II), ς, is 515 cm^{-1} [61]. ΔE_1 is the energy of the lowest doublet state, ^{2}E, arising from the promotion of an electron from d_{xz} or d_{yz} to d_{z^2}. Similarly, ΔE_3 corresponds to the low-lying quartet state ^{4}E′ with the promotion $d_{xz}(\uparrow)$ or $d_{yz}(\uparrow)$ to $d_{xy}(\downarrow)$. The doublet state ^{2}E′ complementary to ^{4}E′ is related in energy and gives rise to the approximation in Eq. (14).

The anisotropic EPR data of Co(II)OEP · py may be analyzed with the help of the foregoing description to obtain the 3d and 4s spin densities (given by α_d^2 and α_s^2, respectively) and the ^2E and $^2E'$ excited state energies relative to the $^2A_{1_g}$ ground state. These results are presented in the upper left-hand portion of Table 4, referred to as the deoxy precursor. The values of the main parameters (α's and E's) of the model reproduce the experimentally observed principal values of the g and ^{59}Co hf tensor. This analysis indicates that 97.5% of the upe

Table 4. Simulation of the principal values of the g tensor and ^{59}Co hf tensor (MHz) for Co(II)OEP · py · $O_2^{-\bullet}$ and $B_{12r}O_2^{-\bullet}$ and their respective deoxy precursors.

	Parameters		Co(II)OEP/ Co(III)OEP · py · $O_2^{-\bullet}$	$B_{12r}/B_{12r}O_2^{-\bullet}$
Deoxy precursor	Electronic structure parameters[a]	α_d^2	0.924	0.812
		α_s^2	0.051	0.067
		ΔE_1 $xz \rightarrow z^2$	8629	8797
		$yz \rightarrow z^2$	8629	11306
		$\Delta E_3'$ $xz \rightarrow xy$	4175	7253
		$yz \rightarrow xy$	4175	9763
	Spin Hamiltonian parameters: calc. (expt.)[b]	g_x	2.326 (2.326)	2.310 (2.310)
		g_y	2.326 (2.326)	2.190 (2.190)
		g_z	2.024 (2.024)	2.004 (2.004)
		A_x (Co)	25 (25)	65 (65)
		A_y (Co)	25 (25)	80 (80)
		A_z (Co)	233 (233)	302 (302)
Superoxo species	Electronic structure parameters[c]	ΔE_u	2096	2113
		ΔE_v	4218	4113
		ΔE_w	4250	4600
		α_2	0.2090	0.1752
		α_3	0.0483	0.0453
		β_2	0.2156	0.2221
	Spin Hamiltonian parameters: calc. (expt.)[d]	$g_{x'}$	2.001 (2.003)	2.001 (2.013)
		$g_{y'}$	2.086 (2.086)	2.089 (2.089)
		$g_{z'}$	1.993 (1.987)	1.993 (1.993)
		A_x (Co)	59 (59)	64.8 (64.8)
		A_y (Co)	26 (26)	30.0 (30.0)
		A_z (Co)	22 (22)	18.7 (18.7)
	Ground state $^2B'$ admixture[e]	CI ($^2B'$) (%)	15.20	13.83
		ΔE_s ($^2B'$)	1107	970
	Spin density analysis[f]	π_a^* (O_2)	+0.2209	+0.1893
		π_b^* (O_2)	+0.7603	+0.7754
		$3d_{yz}$ (Co)	$+3.706 \cdot 10^{-2}$	$+4.023 \cdot 10^{-2}$
		$3d_{z^2}$ (Co)	$-1.151 \cdot 10^{-2}$	$+1.442 \cdot 10^{-3}$
		4s (Co)	$-6.292 \cdot 10^{-3}$	$-5.707 \cdot 10^{-3}$
		Σ out-of-plane (lig)	$-6.21 \cdot 10^{-4}$	$-1.791 \cdot 10^{-3}$
		Σ in-plane (lig)	$+1.64 \cdot 10^{-4}$	$+1.204 \cdot 10^{-3}$

[a] For the definitions of α_d^2, α_s^2, ΔE_1 and $\Delta E_3'$ see text.

[b] A perfect simulation is obtained in both cases; the experimental values for B_{12r} are taken from [33], and the analysis appropriate for C_{2v} symmetry is applied (see [68]).

[c] For definitions of ΔE_u, ΔE_v, ΔE_w and α_2, α_3, β_2, see text. For Co(III)OEP · py · $O_2^{-\bullet}$ ΔE_0 = 19175 cm^{-1} (see text) and the geometric paramters used were R(Co-O_1) = 0.19 nm, R(O_1-O_2) = 0.13 nm and ∠Co-O_1-O_2 = 113°. For $B_{12r}O_2^{-\bullet}$ ΔE_0 = 24763 cm^{-1} (derived from the $3d_{yz}$ value for $\Delta E_3'$ of the deoxy precursor). The geometrical parameters are R(Co-O_1) = 0.19 nm, R(O_1-O_2) = 0.127 nm and ∠Co-O_1-O_2 = 111°.

[d] The low-temperature experimental values for $B_{12r}O_2^{-\bullet}$ are taken from [33]. The experimental $g_{x'}$ value could not be faithfully reproduced by the model. Very small admixtures of other 3d AO's in the 1a MO ($3d_{x^2-y^2}$ and $3d_{xz}$ also transform according to the A irreducible representation) could account for this deviation. Note that for the Co hf tensor an angle of $\alpha = 0°$ was assumed for simplicity in these calculations (see text).

[e] For both cases, a very significant (ca. 15%) admixture of the $^2B'$ state in the ground state wavefunction is estimated. This state is predicted to lie ca. 1000 cm^{-1} (given by ΔE_s, see text) above the ground state.

[f] In both cases, the analysis shows that an almost unit positive spin density resides in the oxygen moiety; the largest metal AO spin density resides in $3d_{yz}$. The sum of the in-plane nitrogen (sp^2 hybrids) densities is positive and less than the magnitude of the out-of-plane (nitrogen and oxygen sp^2 hybrids) sum of spin densities. The total spin density for both the Co(III)OEP · py · $O_2^{-\bullet}$ and $B_{12r}O_2^{-\bullet}$ is calculated to be +1.000, as would be expected.

resides at the metal. The energy of the ^2E excited state, which is known experimentally to be sensitive to the axial field [44, 59], provides a good indicator for the interaction of the complex with the base. The $^4E'$ state provides significant contributions to the spin Hamiltonian parameters and is lower in energy than ^2E. It is, however, less sensitive to the axial ligand field. This information may now be used to elaborate on three aspects of the EPR/ENDOR data of the Co(II) complexes: base-on and -off effects, ligand ^{14}N, ^{15}N ENDOR and ^1H, ^2H ENDOR.

4.1.1 Base-on and -off Effects

Table 1 provides an overview of the various base-on and base-off effects. In the base-off extreme, represented by Co(II)OEP in a Ni(II.OEP host, very large g shift anisotropies occur and, as a result, also a large ^{59}Co hf anisotropy. This is consistent with a much lower ^2E energy as a result of the negligible axial field. A concomitant effect is a smaller 4s admixture in the ground-state wavefunction. (The largely self-cancelling effect of the oppositely signed K_d and K_s is relaxed, thereby causing the observed magnitude of the isotropic part of the ^{59}Co hfc to markedly increase). Species 1 in THF shows analogous behavior to the NiOEP host, consistent with the base-off description. Quantitative analyses of such cases require more rigorous treatments than the perturbation approach in the foregoing section. Co(II)OEP as species 2 in THF, in MeOH plus $CHCl_3$ and in py plus $CHCl_3$ form a series of progressively stronger axial crystal field strengths. As already discussed, the py plus $CHCl_3$ sample is best described as having a single pyridine molecule axially ligated to the Co(II)OEP.* The ENDOR results are discussed on this basis.

---

* In spite of the strong axial field provided by pyridine the complex is only five-coordinated, probably because the Co(II) is pulled out of the plane of the porphyrin ligand, sterically precluding stable sixth ligand coordination. However, oxygenation is no problem since the O_2 molecule is very small.

4.1.2 Ligand Nitrogen ENDOR

As stated in Sect. 3.2.2, the only easily identifiable nitrogen nucleus is that in the pyridine ligand. The nitrogen ENDOR results allow a direct discussion of the spin-density distribution in the AO's of the axially-located nitrogen atom. The hf principal values of ^{15}N reveal a dominant isotropic component (-56.0 MHz) and a small anisotropic part: $+2.0$, $+2.0$, -4.0 MHz for the x, y, z components, respectively. The discussion will therefore focus on the largest unique component (z) and assume an approximately axial character.

The major contribution to the isotropic component will arise from a positive spin density in the nitrogen 2s AO (ρ_{2s}), being a component of the pyridine lone pair orbital which overlaps directly with the cobalt $3d_{z^2}$ AO. The negative sign of the isotropic hfs is inferred on this basis. The isotropic splitting from a unit 2s density for ^{14}N has been estimated [62], and the corresponding value for ^{15}N may be deduced with the ratio of their respective nuclear moments. The experimental isotropic component corresponds to $\rho_{2s} = 0.026$. The anisotropy arises mainly from the dipolar interaction of the density in the nitrogen $2p_z$ AO (ρ_{2p}) with the nuclear moment, with a significant additional contribution from the almost unit density centered at the cobalt atom. This latter contribution provides approximately $+1$, $+1$, -2 MHz (x, y, z) for an estimated Co-N bond length of 0.2 nm. The remainder, which is dependent on ρ_{2p}, corresponds to a value for $\rho_{2p} = 0.018$. The ratio $\rho_{2s}/\rho_{2p} = 1.44$ is in contradiction to that expected (0.5) for an sp^2 hybridized lone pair, and may be contrasted to the axial Co-N situation found in vitamin B_{12r} [33], where a value of 0.63 is determined. (These authors neglect to mention whether a correction for the cobalt spin-density contribution was included). The total density at the nitrogen ($+0.044$) is not inconsistent with a total of $+0.975$ for the AO's of the cobalt atom, since several small positive and negative spin densities are also expected at other ligand locations.

The hf principal values derived from the ^{14}N ENDOR data are consistent with the ^{15}N results. As pointed out above, no reliable ^{14}N quadrupole couplings could be deduced for CoOEP · py. For the system CoTPP · py Däges and Hüttermann [8] and van Doorslaer et al. [9] reported values that show the right ordering and are in approximate agreement with theoretical predictions [63, 64]. The analysis shows that the largest (negative) quadrupole tensor component lies along the Co-N(py) bond and that the asymmetry parameter is $\eta \approx 0.3$. The earlier estimate for these values deduced from the ^{14}N ENDOR spectra [51, 56] of $+1.4$, -0.5, -0.9 (x, y, z) is obviously not correct. This was probably caused by an erroneous assignment of the ^{14}N ENDOR lines.

4.1.3 Ligand Proton ENDOR

The hfs data of the three groups of protons identified have been summarized in Table 2. They display very small isotropic and anisotropic couplings, whose magnitudes decrease with increasing distance of the observed proton from the

metal, i.e., ortho-(py) > meso(OEP) > ethyl(OEP). Our previous EPR/ENDOR powder study [39] on axially ligated Co(II)dmgH_2 complexes has shown that the anisotropy is almost exclusively determined by the dipolar interaction between the bulk spin density at the cobalt atom and the distant proton. Not only could the spatial location of the protons in the axes system of the *g* tensor be determined, but also coupling constant sign ambiguities could be usefully resolved.

The geometrical parameters of the pyridine ortho-protons are consistent with the pyridine molecule being axially bound, such that its plane is perpendicular to the *xy*-plane. The two planes intersect in a line estimated to lie 22° from one of the in-plane axes. The isotropic hfc corresponds to $\rho_{1s} = +6 \cdot 10^{-4}$, and may arise through polarization of the intermediate σ framework by unpaired spin density in the nitrogen lone pair orbital, or spin-orbit admixture of $3d_{xz}$, weakly overlapping directly with the ortho-hydrogen 1s orbital. Spin-orbit admixture of $3d_{yz}$ back-bonding to the pyridine π^* system, followed by polarization of the C-H bond seems unlikely since this would produce a negative spin density at the hydrogen nucleus.

The same general comments can be advanced for both the meso- and ethyl-protons on the OEP frame. Their spatial locations are consistent with the accepted OEP geometry. The small negative isotropic hfc for the meso-protons suggests that a polarization mechanism is responsible for its occurrence. One such mechanism could occur, if the cobalt atom lies slightly above the plane of the OEP, as expected. The strict orthogonality between $3d_{z^2}$ and the π orbitals of the OEP would then be lost, thereby allowing a leakage of positive spin density into these delocalized MO's, and ultimately causing a negative density in the meso-H 1s AO by polarization of the C-H σ-bond. This, however, is not the only route by which negative spin density at the meso-proton can be produced.

4.2 The Electronic Structure of Co(III)OEP · py · $O_2^{-\bullet}$

The EPR parameters of the oxygen adduct are similar to those found for a large range of cobalt superoxo complexes [31]. Their dependence on the Co(III) · $O_2^{-\bullet}$ electronic structure may be discussed in terms of the anticipated ordering of MO levels shown in the center of Fig. 11 and two axis systems: that of the parent square planar cobalt(II) complex (*x*, *y*, *z*) and that of the O_2 moiety (*x′*, *y′*, *z′*).

The O_2 *z′*-axis and the Co(II) *y*-axis are collinear and define the normal to the single plane of reflection (*x′y′*) characterizing the C_s point group symmetry of the Co(III) · $O_2^{-\bullet}$ complex. The MO's are distinguished according to their transformation behavior; the three most relevant orbitals [29] are labeled 1a, 2a (transforming as the A irreducible representation) and 1b (transforming as A′).

Two principal models have been put forward to explain the EPR parameters of Co(III) · $O_2^{-\bullet}$ complexes. The "spin-pairing" model introduced by Tovrog et al. [29] proposes that the anisotropic ^{59}Co hfs arises from spin-polarization in the cobalt $3d_{z^2}$ and 4s components of the 1a MO. The "π-back-bonding" model of Hoffman et al. [30] maintains that admixture of cobalt $3d_{yz}$ in the 1b MO provides a direct mechanism. Smith and Pilbrow [31] have sought to include both

mechanisms in their treatment. All these treatments suffer from a number of shortcomings. Firstly, whilst the anisotropic ^{59}Co hfs may be well understood, the isotropic part cannot be consistently accounted for. Secondly, no serious attempt has thus far been made to quantitatively explain the principal values of the *g* tensor. Finally, in the treatment by Smith and Pilbrow [31] there is the unfortunate situation that the number of parameters required by the model exceeds the number of experimental quantities available to determine them.

To circumvent the first of these difficulties, we have already described a successful alternative [53] embodying a more rigorous assessment of the $3d_{z^2}$ and 4s polarization. This approach is now elaborated upon, with a view to tackling the two remaining difficulties. To deal with the quantitative assessment of the various contributions, some remarks regarding the electronic structure modification in going from the Co(II) to Co(III) $\cdot$ $O_2^{-\bullet}$ must be made. The relative placements of the levels in the schemes shown in Fig. 11 are derived on the basis of doublet excitations relative to their respective ground-state configurations. Thus, for example, in the Co(II)OEP $\cdot$ py complex, the $^2E'$ excitation ($3d_{xz}$, $3d_{yz} \rightarrow 3d_{xy}$) is estimated at 15000 cm^{-1} [44] above the corresponding $^4E'$ excitation at ca. 19000 cm^{-1}. The mainly $3d_{x^2-y^2}$ MO is expected to lie below the $3d_{xz}$, $3d_{yz}$; were sixfold coordination to be completed, the $3d_{xz}$, $3d_{yz}$ and $3d_{x^2-y^2}$ orbitals would attain a more degenerate disposition.

We assume at the outset that this is the case in the dioxygen adduct and, since there are no in-plane coordination changes, the coarse $3d_{x^2-y^2}$, $3d_{xz}$, $3d_{yz}$ to $3d_{xy}$ separation is the same as that for the $3d_{xz}$, $3d_{yz}$ to $3d_{xy}$ separation (defined as ΔE_0) estimated for the deoxy precursor. The placement of the three relevant MO's: 1a, 1b and 2a within these limits may be characterized by parameters ΔE_u, ΔE_v and ΔE_w. They correspond to doublet excited states having the configurations $(1a)^1(1b)^2$, $(1a)^2(2a)^1$, and $(1a)^2(3d_{xy})^1$, respectively. The energies of higher excited states arising from $(3d_{x^2-y^2})^1(1a)^2(1b)^2$, $(3d_{xy})^1(1a)^2(1b)^2$ and $(3d_{xz})^1(1a)^2(1b)^2$ configurations may be coarsely estimated from the foregoing to assess the less important spin-orbit contributions to the *g* and ^{59}Co hf tensors. The 1a, 1b and 2a MO's require a more precise description; under the assumption of C_s symmetry their important components are:

$$|2a\rangle = \gamma_1 |\phi_{z^2}\rangle - \gamma_2 |\pi_a^*\rangle , \tag{15}$$

$$|1b\rangle = \beta_1 |\pi_b^*\rangle - \beta_2 |3d_{yz}\rangle , \tag{16}$$

$$|1a\rangle = \alpha_1 |\pi_a^*\rangle + \alpha_2 |\phi_{z^2}\rangle + \alpha_3 |\phi_s\rangle . \tag{17}$$

The major components of the 1a and 1b MO's, π_a^* and π_b^* respectively, are the antibonding π MO's of an unperturbed oxygen molecule. The major component of the 2a MO is ϕ_{z^2} which takes the same metal and ligand orbital composition as the MO of mainly $3d_{z^2}$ character determined for the deoxy precursor. ϕ_s is assumed to take a composition which complements that of ϕ_{z^2}. The function becomes:

$$|\phi_s\rangle = \alpha_d|4s\rangle - \alpha_s|3d_{z^2}\rangle - \alpha_l|lig'\rangle . \quad (18)$$

The coefficients are related to those of ϕ_{z^2}. The ligand component, denoted by $|lig'\rangle$, has a different character than $|lig\rangle$, but for a first approximation is assigned the same coefficient. The $|lig\rangle$ and $|lig'\rangle$ are assumed to be group orbitals comprising the six lone pair hybrid atomic orbitals directed towards cobalt from the five nitrogen atoms and single oxygen atom attaching the in-plane and and out-of-plane ligands. Their approximate composition is assumed to be governed by the principle of maximum overlap with $3d_{z^2}$ and 4s, respectively, i.e., $|lig\rangle = (1/\sqrt{3})(\sigma_1 + \sigma_2) - (1/\sqrt{12})(\sigma_3 + \sigma_4 + \sigma_5 + \sigma_6)$ and $|lig'\rangle = (1/\sqrt{6})\times(\sigma_1 + \sigma_2) + (1/\sqrt{6})(\sigma_3 + \sigma_4 + \sigma_5 + \sigma_6)$, where σ_1, σ_2 come from the out-of-plane ligands, and σ_3, σ_4, σ_5 and σ_6 from the in-plane ligands. This rather crude approximation serves to maintain orthonormality of ϕ_{z^2} and ϕ_s, and is necessary for making a coarse estimate of the hf characteristics of the pyridine nitrogen nucleus at a later stage. Approximate orthonormalization determines the dominant coefficients α_1, β_1, γ_1, and the coefficient γ_2 in terms of α_2, α_3 and β_2.

The obvious near-degeneracy of the 1a and 1b oxygen-based MO's and their close location to the 2a metal-based MO already provides a situation where the ground state may not be well described in terms of a single determinant wavefunction. ^{17}O-substitution experiments on $B_{12r}O_2^{-\bullet}$ [33] determined a significant spin density in the oxygen AO's of the same symmetry as the 1a MO in our notation and supports this case. Such a characteristic will markedly affect the ^{59}Co hf contributions. We, therefore, adopt the simplest description of the ground state to accommodate this additional possibility.

In the three-orbital scheme with C_s symmetry, configuration interaction (CI) arguments [65] show that the ground state

$$|^2B\rangle = ||\,1a\,\overline{1a}\,1b\,|| \quad (19)$$

is perturbed by just two singly-excited doublet configurations and only one of these:

$$|^2B'\rangle = \frac{2}{\sqrt{6}}||\,1a\,\overline{1b}\,2a\,|| - \frac{1}{\sqrt{6}}||\,1a\,1b\,\overline{2a}\,|| - \frac{1}{\sqrt{6}}||\,\overline{1a}\,1b\,2a\,||\,, \quad (20)$$

leads to spin polarization. The zero-order energy of this state, relative to ^2B, may be related to ΔE_u and ΔE_v [53, 65], the corresponding energies of the simpler doublet excitations, 1a → 1b and 1b → 2a, respectively:

$$\Delta E_s = \Delta E_u + \Delta E_v + J_{1a1b} + J_{1b2a} - J_{1b1b} - J_{1a2a} - \frac{1}{2}K_{1a1b} - \frac{1}{2}K_{1b2a}\,, \quad (21)$$

where, for example, J_{1a1b} and K_{1a1b}, respectively, represent the Coulomb and exchange integrals between electrons in the 1a and 1b MO's. Interaction of the states under the many-electron Hamiltonian [66] is given by

$$\langle {}^2\mathrm{B}|\mathscr{H}|{}^2\mathrm{B}'\rangle = -\sqrt{\frac{3}{2}}\,\langle 1\mathrm{a}(1)1\mathrm{b}(2)|er_{12}^{-1}|1\mathrm{b}(1)2\mathrm{a}(2)\rangle$$
$$= \sqrt{\frac{3}{2}}\,\alpha_1\gamma_2\beta_1^2 K(\pi_\mathrm{a}^*\pi_\mathrm{b}^*)\,. \tag{22}$$

The standard procedures applied in MO calculations [67] may be used to estimate the various Coulomb and exchange integrals as functions of MO coefficients and Co-O-O geometry. With this information, an improved ground-state wavefunction

$$\Psi_{^2\mathrm{B}} = \sqrt{1-\lambda^2}\;|{}^2\mathrm{B}\rangle + \lambda|{}^2\mathrm{B}'\rangle \tag{23}$$

may be estimated.

Clearly, admixture of the low-lying $^2\mathrm{B}'$ state introduces nonvanishing spin density in the oxygen π_a^* orbital, the metal $3\mathrm{d}_{z^2}$ and 4s AO's and both the porphyrin in-plane (ip) and the pyridine out-of-plane (op) nitrogen lone pair orbitals. In addition, the spin densities in the π_b^* orbital and $3\mathrm{d}_{yz}$ AO are no longer given by their respective squared coefficients. The expressions for all these spin densities become:

$$\rho(\pi_\mathrm{a}^*) = -\sqrt{\frac{8}{3}}\,\lambda\sqrt{1-\lambda^2}\;\alpha_1\gamma_2 + \frac{2}{3}\lambda^2(\alpha_1^2+\gamma_2^2)\,, \tag{24}$$

$$\rho(\pi_\mathrm{b}^*) = \left(1-\frac{4}{3}\lambda^2\right)\beta_1^2\,, \tag{25}$$

$$\rho(3\mathrm{d}_{yz}) = \left(1-\frac{4}{3}\lambda^2\right)\beta_2^2\,, \tag{26}$$

$$\rho(3\mathrm{d}_{z^2}) = \sqrt{\frac{8}{3}}\,\lambda\sqrt{1-\lambda^2}\;\gamma_1\alpha_\mathrm{d}(\alpha_2\alpha_\mathrm{d}-\alpha_3\alpha_\mathrm{s})$$
$$+\frac{2}{3}\lambda^2\{\gamma_1^2\alpha_\mathrm{d}^2+(\alpha_2\alpha_\mathrm{d}-\alpha_3\alpha_\mathrm{s})^2\}\,, \tag{27}$$

$$\rho(4\mathrm{s}) = \sqrt{\frac{8}{3}}\,\lambda\sqrt{1-\lambda^2}\;\gamma_1\alpha_\mathrm{s}(\alpha_2\alpha_\mathrm{s}+\alpha_3\alpha_\mathrm{d})$$
$$+\frac{2}{3}\lambda^2\{\gamma_1^2\alpha_\mathrm{s}^2+(\alpha_2\alpha_\mathrm{s}+\alpha_3\alpha_\mathrm{d})^2\}\,, \tag{28}$$

$$\rho_\mathrm{op} \approx \alpha_1^2\left\{\sqrt{\frac{8}{27}}\,\lambda\sqrt{1-\lambda^2}\;\gamma_1(2\alpha_2+\sqrt{2}\,\alpha_3)\right.$$
$$\left.+\frac{2}{9}\lambda^2[2\gamma_1^2+2\alpha_2^2+\alpha_3^2+\sqrt{2}\,\alpha_2\alpha_3]\right\}\,, \tag{29}$$

$$\rho_{ip} \approx \alpha_1^2 \left\{ \sqrt{\frac{8}{27}}\, \lambda \sqrt{1-\lambda^2}\, \gamma_1 (\alpha_2 - \sqrt{2}\, \alpha_3) + \frac{2}{9} \lambda^2 (\gamma_1^2 + \alpha_2^2 + 2\alpha_3^2 - \sqrt{2}\, \alpha_2 \alpha_3) \right\} . \quad (30)$$

The expression for the in-plane (OEP) spin density represents the sum for all nitrogen atoms.

Taking account of the definitions of the various coefficients (Eqs. (15)–(17)) and their expected relative magnitudes, the sign of the admixture coefficient, λ, is predicted to be negative. This further implies a positive spin density in the oxygen π^* orbital and the $3d_{yz}$ orbital. In the other orbitals the sign of the spin densities depends on the relative magnitudes of the various contributions. The sum of the spin densities given by Eqs. (24)–(30) is exactly unity.

For a given Co-O-O geometry, the ground state is determined by six parameters: ΔE_u, ΔE_v, ΔE_w, α_2, α_3, and β_2. The various individual contributions to the g tensor and the ^{59}Co hf tensor are analyzed in detail in Appendix. A computer program was written to calculate the principal values of these tensors for different trial values of the six foregoing parameters; the deoxy precursor data and the Co-O-O geometry were held constant. The parameter values required to get the best overall fit to the experimental data are presented in the bottom half of Table 4 in the superoxo complex section. For comparison purposes, and to demonstrate the wider application of this approach to other superoxo Co(III)$\cdot O_2^{-\bullet}$ complexes, a complementary analysis with data for vitamin B_{12r} [68] and vitamin $B_{12r}O_2^{-\bullet}$ [33] are presented on the right-hand side of Table 4.

The foregoing reasoning regarding the relevant components of the MO's and the energetic placement of the important levels allows the model to reproduce the six observables (the principal values of the g and ^{59}Co hf tensors) for reasonable values of the six unknown parameters. With the aid of Eqs. (24)–(30), these parameters can be used to reconstruct the main spin distribution between the metal and the oxygen fragments. These values are presented at the bottom of Table 4. This analysis shows that the bulk of the spin density is removed to the oxygen fragment with positive densities in both the π_a^* and π_b^* orbitals. The largest spin density at the metal resides in the $3d_{yz}$ AO; it is positive and is only 5% of the total oxygen spin density. Negative spin densities of smaller magnitudes reside in the $3d_{z^2}$ and 4s AO's.

Although ^{17}O experiments were beyond the scope of this work, the study by Jörin et al. [33], used as the second example for our analysis (see Table 4), reported the determination of the ^{17}O hf tensors for both oxygen atoms. For $B_{12r}O_2^{-\bullet}$ we also estimate a positive spin density for both the π_a^* and π_b^* oxygen orbitals. This disagrees with their conclusion that the sign of the spin density in π_a^* is negative; their analysis yielded a ratio of the spin density magnitudes, $|\rho_a|/|\rho_b| = 0.25$. Their conclusion, however, is dependent on the assumption that the measured ^{17}O hf component along our z'-axis is positive. The alternative sign choice yields a ratio of 0.32 ± 0.10, which would not be in conflict with the result of 0.25, predicted by our model.

4.2.1 Ligand Nitrogen ENDOR

As discussed in Sect. 3.3.2, the hf and nuclear quadrupole tensors for ^{14}N could not be determined accurately. The ^{15}N results, however, yielded details of the hf tensor. Equation (29) shows that the spin density resident in the nitrogen lone-pair orbital is proportional to α_1^2 and, therefore, proportional to that of the Co(II) precursor. The reduction factor relating these two cases is estimated from the model to be ca. $4 \cdot 10^{-2}$. This directly predicts an isotropic hfs of ca. 2.2 MHz with anisotropic variations of ≤ 0.2 MHz. This is in reasonable agreement with the experimental value of $A_{iso} = 3.6$ MHz and the almost isotropic behavior of the spectrum.

4.2.2 Ligand Proton ENDOR

Only the hfc's of the ortho- and meta-protons on pyridine are clearly determined by ENDOR. The isotropic component is reduced by about 25% compared with the Co(II) precursor, indicating that spin density invades the pyridine C-H bonds to roughly the same small extent in both species. Further, it would seem that the route does not involve the pyridine nitrogen lone-pair orbital whose marked reduction in spin density in the $Co(III) \cdot O_2^{-\bullet}$ has already been discussed. In contrast, the anisotropic components experience a more marked reduction to about 50% of their former value. This is consistent with the bulk of the spin density being located further away at the oxygen moiety. An estimate of the reduction on the basis of the spin-density distribution provided by the model yields 40% of the Co(II) values, in fair agreement with that observed.

5 Conclusions

In this work we have measured the hf interaction parameters of the title compounds, without having recourse to single-crystal dilution in diamagnetic matrix. We have detected ^{59}Co, ^{14}N, ^{15}N and ^{1}H nuclei and their hf data by ENDOR. The direct comparison with the superoxo form allows a detailed analysis of spin density distribution, the relative energies of the MO's and MO coefficients, and we can draw very precise conclusions on the structural/geometrical alignment. This knowledge would also allow understanding of the function of oxygen activation both in natural and artificial systems and could be used to regulate catalytic processes [25, 69].

Appendix

The leading contributions to the g tensor, in the axis system of the oxygen molecule (x', y', z'), and the ^{59}Co hf tensor, in the axis system of Co(II)OEP-py (x, y, z), are derived as follows.

The *g* tensor. The principal values of the g tensor may be best assessed by regarding the Co(III)OEP · py · $O_2^{-\bullet}$ complex as a perturbed superoxide ion ($O_2^{-\bullet}$) in which the π_a^*, π_b^* degeneracy is removed. The anisotropic g shifts ($\Delta g_i = g_i - g_e$; $i = x', y', z'$) primarily reflect the energetic disposition of spin-orbit coupled levels with respect to the π_a^* orbital. For example, the major part of the largest shift, $\Delta g_{y'}$, is inversely proportional to the $|1a\rangle$, $|1b\rangle$ separation. For $\Delta g_{x'}$, spin-orbit coupling between π_b^* and the σ^*, n, n' MO's of the O_2 leads to contributions of the respective opposite signs. Indeed, $O_2^{-\bullet}$ occluded in various zeolite matrices [70] and in a freely solvated form [29] show that $g_{x'} \approx 2.00$, indicating a rather complete cancellation. For $\Delta g_{z'}$, no significant contributions are expected (since $\mathbf{L}_{z'}|2p_{z'}\rangle = 0$), and this situation is also observed.

In the Co(III)OEP · py · $O_2^{-\bullet}$ complex, the foregoing coarse assessment will be modified as a result (a) of the new multi-configuration nature of the ground state and (b) the involvement of metal orbitals. The contributions may be outlined as follows:

^{2}B state, O_2 contributions:

$$\delta_{x'} = 0\,, \tag{A1}$$

$$\delta_{y'} = (1 - \lambda^2)\beta_1^2\zeta(O_2)\left\{\frac{d_1^2}{\Delta E_u} - \frac{\gamma_2^2}{\Delta E_v}\right\}, \tag{A2}$$

$$\delta_{z'} = 0\,, \tag{A3}$$

where $\zeta(O_2)$ is the spin-orbit coupling constant for oxygen.

^{2}B state, Co contributions:

$$\delta_x = (1 - \lambda^2)(-6\eta_3 + 2\eta_4)\,, \tag{A4}$$

$$\delta_y = (1 - \lambda^2)(-2\eta_1)\,, \tag{A5}$$

$$\delta_z = (1 - \lambda^2)(2\eta_2)\,. \tag{A6}$$

For the B_2 state, the coefficients $\eta_1 \ldots \eta_4$ are defined by analogy to McGarvey's treatment of a $(d_{yz})^1$ ground state [44]. They include the factor $(1 - \lambda^2)\beta_2^2$ for η_1, η_2 and η_4, and the factor $(1 - \lambda^2)\beta_2^2\gamma_1^2\alpha_\delta^2$ for η_3. Note that the signs of the η_3 terms are reversed, since the 2a MO with mainly $3d_{z^2}$ character is now unoccupied in this ^{2}B state. Thus, $\eta_1 \ldots \eta_4$ can be estimated in terms of the MO coefficients and energy separation parameters.

Contributions from the admixed B_2' state are neglected. Examination of the leading terms shows that these are less significant, either by virtue of $\lambda^2 \ll 1$, or because the relevant energy denominators become too large. The latter can only be coarsely estimated; no experimental data for the excited states involved exists. The metal orbital contributions may now be re-expressed in the O_2 axis

system according to the orbital angular momentum transformation dependence, but neglecting gauge differences. The tensor elements become:

$$g_{x'x'} = g_e + \delta_x \sin^2\alpha + \delta_z \cos^2\alpha\,, \tag{A7}$$

$$g_{y'y'} = g_e + \delta_{y'} + \delta_x \cos^2\alpha + \delta_z \sin^2\alpha\,, \tag{A8}$$

$$g_{z'z'} = g_e + \delta_y\,, \tag{A9}$$

$$g_{x'y'} = (\delta_x - \delta_z)\cos\alpha\sin\alpha\,, \qquad g_{x'z'} = g_{y'z'} = 0\,. \tag{A10}$$

The ^{59}Co hf tensor. There are three important contributions to the ^{59}Co hf tensor, namely: (i) direct contributions arising from $3d_{yz}$ admixtures in $|1b\rangle$; (ii) polarization resulting from CI with the $^2B'$ excited state, and (iii) pure dipolar contributions from localized bulk spin density on O_2.

Contributions to the tensor will be derived in the metal x, y, z axis system. Off-diagonal elements are zero for mechanisms (i) and (ii) and insignificantly small for (iii); therefore, only diagonal elements will be considered.

(i) Direct $3d_{yz}$ contributions. With appropriate modification, we draw on the expressions of McGarvey [44] for a $(d_{yz})^1$ ground state, neglecting quartet excited states and terms higher than first order.

$$xx\text{:}\quad \left(K_d - \frac{4}{7}P\right)\rho(3d_{yz}) + P\left(-\frac{3}{7}\eta_1 + \frac{3}{7}\eta_2 - 6\eta_3 + 2\eta_4\right), \tag{A11}$$

$$yy\text{:}\quad \left(K_d + \frac{2}{7}P\right)\rho(3d_{yz}) + P\left(-2\eta_1 - \frac{3}{7}\eta_2 + \frac{3}{7}\eta_3 + \frac{3}{7}\eta_4\right), \tag{A12}$$

$$zz\text{:}\quad \left(K_d + \frac{2}{7}P\right)\rho(3d_{yz}) + P\left(\frac{3}{7}\eta_1 + 2\eta_2 - \frac{3}{7}\eta_3 - \frac{3}{7}\eta_4\right). \tag{A13}$$

The same remarks concerning $\eta_1 \ldots \eta_4$ are valid as for the g-tensor expressions. $\rho(3d_{yz})$ is given by Eq. (26).

(ii) Polarization contributions via $^2B_2'$. Admixture of the low-lying $^2B'$ introduces non-vanishing $3d_{z^2}$ and 4s spin densities in the ground state. The expressions for $\rho(3d_{z^2})$ and $\rho(4s)$ are given by Eqs. (27) and (28) in the text.

$$xx\text{:}\quad K_s\rho(4s) + \left(K_d - \frac{2}{7}P\right)\rho(3d_{z^2})\,, \tag{A14}$$

$$yy\text{:}\quad K_s\rho(4s) + \left(K_d - \frac{2}{7}P\right)\rho(3d_{z^2})\,, \tag{A15}$$

$$zz: \quad K_s\rho(4s) + \left(K_d + \frac{4}{7}P\right)\rho(3d_{z^2}), \tag{A16}$$

where here only the dipolar contributions are included. Nuclear spin-orbit contributions are neglected for the same reasons as given in the *g* tensor discussion.

(iii) Dipolar contribution from O_2 spin density. The effect of bulk spin density ρ_i located at each oxygen atom O_i (i = 1, 2) with polar coordinates (ρ_i, θ_i, ϕ_i) in the Co(II) axis system, is as follows. Spin density at O_1, which is assumed to lie on the Co(II) *z*-axis, yields only non-zero contributions to elements of the ^{59}Co hf tensor which are diagonal in the Co(II) axis system. These are:

$$xx: \quad -g_e\beta_e g_n\beta_n\rho_1\left\langle\frac{1}{r_1^3}\right\rangle, \tag{A17}$$

$$yy: \quad -g_e\beta_e g_n\beta_n\rho_1\left\langle\frac{1}{r_1^3}\right\rangle, \tag{A18}$$

$$zz: \quad 2g_e\beta_e g_n\beta_n\rho_1\left\langle\frac{1}{r_1^3}\right\rangle. \tag{A19}$$

For O_2, which is assumed to lie in the metal *xz*-plane (i.e., $\theta_2 \neq 0$, $\phi_2 = 0$), the corresponding contributions are:

$$xx: \quad g_e\beta_e g_n\beta_n\rho_2\left\langle\frac{3\sin^2\theta_2 - 1}{r_2^3}\right\rangle, \tag{A20}$$

$$yy: \quad g_e\beta_e g_n\beta_n\rho_2\left\langle-\frac{1}{r_2^3}\right\rangle, \tag{A21}$$

$$zz: \quad g_e\beta_e g_n\beta_n\rho_2\left\langle\frac{3\cos^2\theta_2 - 1}{r_2^3}\right\rangle, \tag{A22}$$

and an additional non-zero off-diagonal contribution:

$$xz: \quad g_e\beta_e g_n\beta_n\rho_2\left\langle-\frac{3\cos\theta_2\sin\theta_2}{r_2^3}\right\rangle. \tag{A23}$$

For a typical geometry: Co-$O_1 \parallel z$, Co-O_1-O_2 in the *xz*-plane with r_{CoO_1} = 1.9 Å, $r_{O_1O_2}$ = 1.3 Å, ∠Co-O_1-O_2 = 113° the following coordinates are estimated: r_1 = 1.9 Å, $\theta_1 = 0$ and r_2 = 2.69 Å, θ_2 = 26.4°. Further, the fraction of spin density

on the O_2 moiety located at the oxygen atom bound to cobalt has been estimated in other studies [33] to be 47%.

The *xz* component arising from spin density at O_2 is the only nonzero off-diagonal contribution to the Co^{59} hfs. It is much smaller than the difference between the relevant pair of final diagonal elements (*xx* and *zz*), and can reasonably be neglected. This means that the principal axes of the Co^{59} hfs tensor in the $Co(III) \cdot O_2^{-\bullet}$ complex are very nearly those of the Co(II) precursor.

Acknowledgements

The authors are grateful to Dr. M. Plato and Dr. F. Lendzian for their help concerning theoretical questions and technical details of the instrumentation, to Dr. B. Kirste for computational help and to Dr. R. Bittl who performed part of the EPR simulations; M. Baumgarten is grateful to Prof. Dr. H. Kurreck for the use of his EPR equipment and to Prof. Dr. J.-H. Fuhrhop who provided the octaethylporphyrin. This project was supported by the Deutsche Forschungsgemeinschaft and by the Fonds der Chemischen Industrie (W. Lubitz, M. Baumgarten).

References

1. Basolo F., Hoffman B.M., Ibers J.A.: Acc. Chem. Res. **1975**, 384–392.
2. Drago R.S.: Coord. Chem. Rev. **32**, 97–110 (1980)
3. Subramanian J. in: Porphyrins and Metalloporphyrins (Smith K.M., ed.), pp. 555–589. Amsterdam: Elsevier 1975.
4. Sheldon R.A., Kochi J.K.: Metal Catalyzed Oxidations of Organic Compounds. New York: Academic Press 1981.
5. Daul C., Schläpfer C.W., von Zelewsky A.: Structure and Bonding **36**, 129 (1979)
6. Martell A.E. (ed.): Coordination Chemistry, ACS Monograph, vol. 1. New York: Van Nostrand Reinhold Comp. 1971.
7. Walker F.A.: J. Am. Chem. Soc. **95**, 1154 (1973)
8. Däges G.P., Hüttermann J.: J. Phys. Chem. **96**, 4787 (1992)
9. van Doorslaer S., Bachmann R., Schweiger A.: J. Phys. Chem. B **103**, 5446 (1999)
10. van Doorslaer S., Schweiger A.: J. Phys. Chem. B **104**, 2919 (2000)
11. Bowen J.H., Shokhirev N.V., Raitsimring A.M., Buttlaire D.H., Walker F.A.: J. Phys. Chem. B **101**, 8683 (1997)
12. Dolphin D. (ed.): B_{12}. New York: Wiley 1982.
13. Zagalak P., Friedrich W. (eds.): Vitamin B_{12}. Berlin: De Gruyter 1979.
14. Rao R.D.N., Symons M.C.R.: J. Chem. Soc. Perkin Trans. II **1983**, 187; J. Chem. Soc. Faraday Trans. I **79**, 269 (1983)
15. Bayston J.H., King N.K., Looney F.D., Winfield M.E.: J. Am. Chem. Soc. **91**, 2775 (1969)
16. Jörin E., Schweiger A., Günthard Hs.H.: Chem. Phys. Lett. **61**, 228 (1979)
17. James B.R. in: The Porphyrins (Dolphin D., ed.), vol. 5, pp. 207 ff. New York: Academic Press 1979.
18. Jones R.D., Summerville D.A., Basolo F.: Chem. Rev. **79**, 139–179 (1979)
19. Spiro T.E. (ed.): Metal Ion Activation of Dioxygen. New York: Wiley 1980.
20. Hill C.J. (ed.): Activation and Functionalization of Alkanes. New York: Wiley 1989.
21. Vigato P.A., Tamburini S., Fenton D.E.: Coord. Chem. Rev. **106**, 25 (1990)
22. Hamilton D.E., Drago R.S., Zombeck A.: J. Am. Chem. Soc. **109**, 374 (1987)

23. Sobkowiak A., Sawyer D.T.: J. Am. Chem. Soc. **113**, 9520 (1991)
24. Suzuki Y., Nishide H., Tsuchida E.: Macromolecules **33**, 2530 (2000)
25. Nishide H., Tsuchida E. in: Macromolecular Complexes (Tsuchida E., ed.), pp. 119 ff. Weinheim: VCH 1991.
26. Chien J.C.W., Dickinson L.C. in: Biological Magnetic Resonance (Berliner L.J., Reuben J., eds.), vol. 3, chap. 4, p. 155. New York: Plenum Press 1981.
27. Dolphin D. (ed.): The Prophyrins, vol. 1–7. New York: Academic Press 1978, 1879.
28. Walker F.A.: J. Magn. Reson. **15**, 201 (1974); Walker F.A., Reis D., Blake V.L.: J. Am. Chem. Soc. **106**, 6888–6898 (1984); Walker F.A., Brown J.: J. Am. Chem. Soc. **107**, 7632 (1985)
29. Tovrog B.S., Kitko D.J., Drago R.S.: J. Am. Chem. Soc. **98**, 5144 (1976)
30. Hoffman B.M., Diemente D.L., Basolo F.J.: J. Am. Chem. Soc. **92**, 61 (1970)
31. Smith T.D., Pilbrow J.R.: Coord. Chem. Rev. **39**, 295–383 (1981)
32. Getz D., Melamud E., Silver B.L., Dori Z.: J. Am. Chem. Soc. **97**, 3846 (1975)
33. Jörin E., Schweiger A., Günthard Hs.H.: J. Am. Chem. Soc. **105**, 4277–4286 (1983)
34. Schweiger A.: Structure and Bonding **51**, 1 (1982)
35. Schweiger A. in: Electron Spin Resonance, vol. 10, 138–185, 1987.
36. Rist G.H., Hyde J.S.: J. Chem. Phys. **52**, 4633–4643 (1970)
37. Möbius K., Lubitz W. in: Biological Magnetic Resonance (Berliner L.J., Reuben J., eds.), vol. 7, chap. 3, pp. 129–247. New York: Plenum Press 1987.
38. Stach J., Böttcher R., Kirmse R.: Z. Chem. **25**, 1 (1985)
39. Baumgarten M., Lubitz W., Winscom C.J.: Chem. Phys. Lett. **133**, 102 (1987)
40. Hurst G.C., Henderson T.A., Kreilick R.W.: J. Am. Chem. Soc. **107**, 7294, 7299 (1985)
41. Greiner S.P., Kreilick R.W., Kraft K.A.: J. Am. Chem. Soc. **114**, 391–399 (1992)
42. Greiner S.P., Rowlands D.L., Kreilick R.W.: J. Phys. Chem. **96**, 9132–9139 (1992)
43. Kirste B., van Willigen H.: J. Phys. Chem. **87**, 781–788 (1983)
44. McGarvey B.: Can. J. Chem. **53**, 2498 (1975); McGarvey B.: Can. J. Chem. **53**, 3791 (1975)
45. Fleischer E.B.: Inorg. Chem. **3**, 493 (1962)
46. Fuhrhop J.H., Smith K.M. in: Porphyrins and Metalloporphyrins (Smith K.M., ed.), p. 757. Amsterdam: Elsevier 1975.
47. Gouterman M. in: The Porphyrins (Dolphin D., ed.), vol. 3, pp. 1–165. New York: Academic Press 1979.
48. Segal B.G., Kaplan M., Fraenkel G.K.: J. Chem. Phys. **43**, 4191 (1965)
49. Kurreck H., Kirste B., Lubitz W. in: Methods in Stereochemical Analysis (Marchand A.P., ed.), chap. 2.4. New York: VCH Publishers 1988.
50. Lendzian F.: Ph. D. Thesis, Freie Universität Berlin, Berlin, Germany 1982.
51. Baumgarten M.: Ph. D. Thesis, Freie Universität Berlin, Berlin, Germany 1988.
52. Winscom C.J., Atherton N.M.: Inorg. Chem. **12**, 383 (1973)
53. Lubitz W., Winscom C.J., Diegruber H., Möseler R.: Z. Naturforsch. **42** a, 970 (1987)
54. Lin W.C.: Inorg. Chem. **19**, 1072 (1980)
55. Iwaizumi M., Ohba Y., Ilda H., Hirayama M.: Inorg. Chim. Acta. **82**, 47–52 (1984)
56. Greiner S.P., Baumgarten M.: J. Magn. Reson. **83**, 630 (1989); Greiner S.P.: Ph. D. Thesis, University of Rochester, Rochester, N.Y. USA, 1987.
57. Lancashire R.L., Smith T.D., Pilbrow J.A.: J. Chem. Soc. Dalton Trans. **1979**, 66.
58. Höhn M., Hüttermann J.: J. Biol. Chem. **257**, 10554 (1982)
59. Clementi E.: J. Chem. Phys. **41**, 295 (1964)
60. Abragam A., Pryce M.H.L.: Proc. R. Soc. London A **206**, 173 (1951)
61. Dunn T.M.: Trans. Faraday Soc. **57**, 144 (1961)
62. Horsefield A., Morton J.R., Rowlands J.R., Whiffen D.H.: Mol. Phys. **5**, 241 (1962)
63. Hsieh Y.-N., Rubenacker G.V., Cheng C.P., Brown T.L.: J. Am. Chem. Soc. **99**, 1384 (1977)
64. Brown T.G., Hoffman B.M.: Mol. Phys. **39**, 1073 (1980)
65. Longuet-Higgins H.C., Pople J.A.: Proc. Phys. Soc. A **68**, 591 (1955)
66. Hinchliffe A.H.: Theor. Chim. Acta **5**, 208 (1966); Hinchliffe A.H., Ali M.A.: Theor. Chim. Acta **5**, 271 (1966)
67. Scholz M., Köhler H.-J.: Quantenchemie, Band 3. Berlin: VEB 1981.
68. Schweiger A., Jörin E., Günthard Hs.H.: Chem. Phys. Lett. **61**, 223 (1979)
69. Duchstein H.-J., Baumgarten M.: Arch. Pharm. **321**, 781–785 (1988)

70. Kasai P.H., Bishop Jr. R.J.: Zeolite Chemistry and Catalysis (Rabo J.A., ed.). ACS Monograph, vol. 171, 350. Washington: American Chemical Society 1976.

Authors' address: Wolfgang Lubitz, Max-Volmer-Institut, Technische Universität Berlin, Str. des 17. Juni 135, 10623 Berlin, Germany